SCALED LUNAR MODULE
JET EROSION EXPERIMENTS

by Norman S. Land and Harland F. Scholl

Langley Research Center
Langley Station, Hampton, Va.

SCALED LUNAR MODULE JET EROSION EXPERIMENTS

By Norman S. Land and Harland F. Scholl

Langley Research Center
Langley Station, Hampton, Va.

Technical Film Supplement L-1043 available on request.

NATIONAL AERONAUTICS AND SPACE ADMINISTRATION

SCALED LUNAR MODULE JET EROSION EXPERIMENTS

By Norman S. Land and Harland F. Scholl
Langley Research Center

SUMMARY

An experimental research program was conducted on the erosion of particulate surfaces by a jet exhaust. These experiments were scaled to represent the lunar module (LM) during landing. A conical cold-gas nozzle simulating the lunar module nozzle was utilized. The investigation was conducted within a large vacuum chamber by using gravel or glass beads as a simulated soil. The effects of thrust, descent speed, nozzle terminal height, particle size on crater size, and visibility during jet erosion were determined.

Results indicate that, from an erosion and visibility standpoint, the best landing mode for a lunar module type of vehicle would involve: site inspection and selection above the incipient erosion height, and a fast descent to the highest drop-in altitude that the vehicle structure could withstand. A slow and cautious descent with hovering just above the lunar surface would greatly increase crater size and impair visibility.

INTRODUCTION

The descent of any soft landing vehicle to the surface of the moon or planets with rarefied atmospheres requires braking by a rocket descent engine. The exhaust from the braking rocket impinging on the lunar or planetary surface can cause erosion, particularly if the surface is particulate in nature. Erosion can lead to undesirable consequences such as cratering that could degrade landing stability, ejected material that could hamper pilot visibility or damage the vehicle, and sufficient alteration of the landing site to degrade scientific experiments. Accordingly, theoretical and experimental investigations of the effects of supersonic jet blasts on particulate surfaces has been underway at Langley Research Center. A theoretical analysis of the erosion of surface particles due to the aerodynamic shear stress caused by an impinging jet flow in an ambient vacuum was published as reference 1. An experimental study (ref. 2) was made to verify the theoretical analysis. These experiments did, in general, substantiate the theory; and, in addition, the scaling problem was discussed. However, the experiments described in reference 2 did not specifically represent any full-size configuration or method of operation.

The lunar module (LM) used in the Apollo program utilizes a retrorocket during landing which must be fired continuously almost to touchdown in order to minimize landing

loads. To define an acceptable landing mode, the effect of jet erosion at low altitudes for the LM configuration was required. Therefore, an experimental model study which specifically represents the LM landing on the lunar surface has been made. The effects of thrust, descent velocity, nozzle terminal height, and particle size for a scaled LM spacecraft have been investigated and the results are presented herein.

SYMBOLS

C_f aerodynamic drag coefficient on exposed particle

c   particle packing factor

D   particle size

g   gravitational acceleration

h   nozzle exit plane height

$k = \gamma(\gamma - 1)M^2$

l length

M   Mach number

m   mass

R   gas constant

r   nozzle radius

T   temperature

t   time

V   velocity

α particle friction angle

γ specific heat ratio

2

θ nozzle exit angle

λ length scale, l_F/l_M

ρ mass density of gas

σ mass density of particle material

Subscripts:

e exit

F full scale

M model

SCALING

In most experimental research involving the use of models, a choice must initially be made concerning the full-size phenomena that the model will reproduce. This choice is usually necessary because the complex combination of physical phenomena involved in the full-size system cannot be reproduced in complete detail by a model. In planning this model study, it was decided to have the model reproduce the following full-size parameters: (1) jet-exhaust flow field geometry, (2) ratio of aerodynamic shear to particle restraint, and (3) ratio of particle density to gas density. If the model does faithfully reproduce the full-scale conditions in these respects, the model should properly simulate transfer of the kinetic energy of the exhaust gas into the surface stresses and into the kinetic energy of dislodged particles. It was arbitrarily assumed that transfer of thermal energy from the LM exhaust gas to the lunar surface would have little effect on the erosion of the surface. Therefore, the model was not required to simulate the lunar-module—lunar-surface thermal situation. Because the details of the lunar surface were unknown, the model particles were varied in size.

The parameters chosen to have the same value for the model and full size are expressed as follows:

$$\gamma(\gamma - 1)M_e^2 \propto \frac{\text{Jet-exit-gas kinetic energy}}{\text{Jet-exit-gas internal energy}} \tag{1}$$

$$\frac{\sigma g D c \tan \alpha}{C_f \rho V^2} \propto \frac{\text{Particle friction restraint}}{\text{Aerodynamic drag force}} \tag{2}$$

$$\frac{\sigma}{\rho} \propto \frac{\text{Particle density}}{\text{Gas density}} \qquad\qquad (3)$$

The parameter of equation (1) was referred to as a hypersonic parameter in the basic theory of reference 1. With no surrounding atmosphere, the distribution of kinetic energy in the expansion region outside the nozzle exit should be the same for the model and the LM if this parameter has the same numerical value for both the model and the LM. Equal values for this parameter for the LM and the model do not restrict the model to using the propellant gas used in the LM; that is, the γ value for model gas and LM gas need not be the same if the model nozzle is designed for a Mach number which compensates for the different values of γ.

The ratio of equation (2) is based on the assumptions: (a) particle dislodgment is caused by the free-stream aerodynamic drag force on a single exposed particle, and (b) a particle is restrained from movement by a static friction force which is proportional to its weight. Use of the same value of the ratio of equation (3) for the LM and the model insures the correct momentum interchange between gas and particles.

Several things concerning these scaling parameters should be noted. The hypersonic parameter (eq. (1)) is in reality twice the ratio of exhaust-gas kinetic energy to exhaust-gas internal energy as pointed out in reference 3. If this parameter has the same value for two different nozzles, the far-field density distribution along the nozzle axis will be the same for both nozzles if for both nozzles $(\gamma - 1)M_e \leqq \theta^{-1}$. This statement is true for both LM and model nozzles.

The far-field condition is defined as: $(h/r_e)(2/(k + 2))^{1/2} \geqq 1$. If these conditions apply, the density along the axis varies inversely as the square of the distance from the nozzle exit. The same value of the parameter of equation (1) for both nozzles does not insure that the exit plume angle will be the same for both nozzles. However, most of the mass and momentum of the jet are contained in a central core. Calculations show that the exhaust plume angle of the LM jet exhausting in a vacuum is approximately 90°, and that of the model nozzle is approximately 62° in an ambient pressure of 1×10^{-4} torr. With regard to the scaling parameter (eq. (2)), it can be seen that a Froude number Dg/V^2 is contained in the parameter. If this is independently maintained, the ratio of particle inertia forces to particle gravity forces would be the same for model and full size and the trajectories of full-size and model particles would be similar. Some intuitive justification for the use of parameter (3) lies in the use of similar parameters in the fields of airplane dynamic stability and airplane wing flutter where aerodynamic energy is transferred to body kinetic energy.

From the preceding list of parameters and the assumption that C_f, c, and $\tan \alpha$ are the same for the model and full-scale conditions, the following expressions for the basic scaling quantities may be obtained:

$$\frac{\text{Length, full scale}}{\text{Length, model}} \equiv \lambda = \frac{(\gamma_M - 1)}{(\gamma_F - 1)} \frac{R_F}{R_M} \frac{\sigma_M}{\rho_M} \frac{\rho_F}{\sigma_F} \frac{g_M}{g_F} \frac{T_F}{T_M} = \frac{\ell_F}{\ell_M} \qquad (4)$$

$$\frac{\text{Time, full scale}}{\text{Time, model}} \equiv \frac{t_F}{t_M} = \lambda \left[\frac{(\gamma_F - 1)}{(\gamma_M - 1)} \frac{R_M}{R_F} \frac{T_M}{T_F} \right]^{1/2} \qquad (5)$$

$$\frac{\text{Mass, full scale}}{\text{Mass, model}} \equiv \frac{m_F}{m_M} = \lambda^3 \frac{\rho_F}{\rho_M} \qquad (6)$$

It should be noted that nozzle exit conditions are used.

The basic decisions to be made in selecting the model test configuration can be seen (eq. (4)) to be: the choice of model particle material σ_M, the choice of a jet gas γ_M and R_M, and the stagnation temperature and pressure. After considerations of convenience (a "cold" gas nozzle), X-ray penetrating power available (particle density and bed depth), and a convenient model size, helium was chosen as a model gas and glass beads were chosen as the particle material.

Once these decisions were made, the numerical values of γ_F, γ_M, R_F, R_M, σ_F (assumed equal to the density of the moon as a whole), and σ_M are fixed. The lunar gravitational acceleration g_F is known and the experiments on earth fix the value of g_M. Since the experiments are intended to simulate the LM landing, the LM nozzle exit conditions at landing fix the values of ρ_F and T_F. The required value of ρ_M can then be calculated from the scaling parameter (eq. (3)) which stipulates that $\sigma_F/\rho_F = \sigma_M/\rho_M$. At this point, only the value of T_M remains to be determined. By using scaling parameter (1), the known full-scale values of γ_F and M_F, and the value of γ_M for the chosen model gas (helium), the required value of M_M is computed. This value of M_M, an average atmospheric temperature for the stagnation temperature (520° R), and helium compressibility relations yield the value of the model exit temperature T_M. These values are given in the following table:

Term	Full-scale value	Model value
γ	1.32	1.67
R, m^2/sec^2 ^{O}K (ft^2/sec^2 ^{O}R)	410 (2440)	2090 (12 430)
σ, kg / m^3 (lb-sec^2/ft^4)	2580 (5.0)	2580 (5.0)
ρ, kg / m^3 (lb-sec^2/ft^4)	1.21×10^{-3} (2.35×10^{-6})	1.21×10^{-3} (2.35×10^{-6})
g, m/sec^2 (ft/sec^2)	1.62 (5.32)	9.81 (32.2)
T_e, ^{O}K (^{O}R)	672 (1209)	85 (153)
M	4.33	2.68

Substitution of these values in the scaling equations (4), (5), and (6) gives:

Length scale:

$$\frac{l_F}{l_M} = 19.6$$

Time scale:

$$\frac{t_F}{t_M} = 10.9$$

Mass scale:

$$\frac{m_F}{m_M} = 7520$$

From these basic scale ratios, the following derived scale ratios can be determined:

Velocity ratio:

$$\frac{(l/t)_F}{(l/t)_M} = 1.80$$

Force ratio:

$$\frac{(ml/t^2)_F}{(ml/t^2)_M} = 1240$$

Acceleration ratio:

$$\frac{(l/t^2)_F}{(l/t^2)_M} = 0.165$$

For example, the full-scale thrust of 11 350 N (2550 lb) (approximately that used for landing) is represented by a model thrust of 9.15 N (2.06 lb).

In this report, all model conditions have been scaled up to full-scale numerical values by the previous scale ratios. Various test values of thrust, descent velocity, terminal height, and particle size simulate corresponding LM variations. The thrust values used do not necessarily represent either a hovering or a constant-descent-speed condition.

Two of the tests were made with gravel instead of with glass beads. The increase in density of the gravel over the glass beads (8 percent) is believed to be negligible insofar as test interpretation is concerned.

More experimental investigations must be made before the validity of the scaling scheme presented here will be completely established.

FACILITIES AND APPARATUS

Facilities

The experiments were conducted in the 60-foot vacuum sphere and the 55-foot-diameter vacuum cylinder at the Langley Research Center. Both facilities were evacuated by large, oil diffusion pumps which were backed by mechanical pumps. The pressure in either facility at the beginning of each test was in the range from 1×10^{-4} to 3×10^{-4} torr.

A photograph of the test apparatus in the 60-foot vacuum sphere is shown in figure 1. The apparatus at the 55-foot vacuum cylinder is shown in figure 2, and a closeup of the soil bed, X-ray machine, and so forth, is given in figure 3.

The nozzle was attached to the lower end of a vertical steel tube which traveled through rollers. Connected to the upper end of the tube was a dashpot mechanism which controlled the descent velocity. The end of the nozzle descent was cushioned by a rubber bumper.

Particles

Glass beads were selected for use as test particles for most of the experiments because of their availability in closely graded sizes at moderate cost. In addition, most of the glass beads are spheres and, therefore, are considered more amenable to theoretical treatment. Gravel was used as the other test particle for two of the experiments.

The size distribution of the batches of particles that were used is shown in figure 4. The data shown were obtained by passing samples that weighed approximately 150 grams through a series of standard sieves. These standard sieves form a system wherein the linear openings of sieves which are adjacent in the series vary as $\sqrt[4]{2}$ (approximately a 19-percent change). Samples were agitated on a sieve shaker for 15 minutes at 800 revolutions per minute. The log-normal distribution of the particles is stated in reference 4 to more often be the case than a normal, or Gaussian, distribution. It can be seen from the data of figure 4 where the data are plotted on logarithmic-probability coordinates, that the particle distributions are not straight lines as would be the case if the log-normal distributions held exactly. Some of the departure from linearity, on these coordinates, is due to weight loss during sieving. This weight loss is greater as the average size of the batch becomes smaller and varies from 2.8 percent to 0.013 percent. The size distributions have been shown to be closer to log-normal than to normal. Average particle sizes for the batches were: 70, 106, 210, 318, 490, 580, 1000, and 1300 micrometers (model size) and each bed of particles used in the tests is referred to by its average size multiplied by the length scale factor.

The specific gravity of samples of the glass beads has been measured by a liquid displacement method (ASTM C 188-44 (ref. 5)). There was little spread in the data and the average specific gravity was found to be 2.5. The specific gravity of the gravel was determined by the same method (but by use of a nonstandard apparatus) and was found to be 2.7.

Photographs of samples of the particles are shown in figure 5. A 10.2-centimeter-deep (4-inch) bed of particles was used for all tests. This bed of particles represents a 1.99-meter (78.3-inch) depth of lunar soil.

Nozzles

Two nozzles were used for the tests. One was conical with a half-cone angle of 15°. The other had an isentropic contour. Both nozzles were designed for helium, had an exit Mach number of approximately 2.68, and had circular-arc entrance bells and a plenum chamber with a diameter of 19.9 centimeters (7.83 inches). Dimensions of the nozzles are given in figures 6 and 7.

The rocket nozzle used on the LM descent engine is bell-shaped and has a lip angle of 9.8^O. This shape was derived by optimization, weight, length, and thrust being the major considerations. Because the model would use cold helium ($\gamma = 1.67$) and not the hot propulsion gases of the LM ($\gamma = 1.32$), the shape of the LM nozzle would probably have no particular merit for the model. Therefore, the nozzle used for most of the model studies was a simple conical shape with a half-angle of 15°. Another nozzle with a long isentropic shape was also constructed but was not used for many of the tests because the extreme length severely limited the descent distance with the available apparatus.

Instrumentation

Instrumentation was used to record during each test run: (1) the gas state conditions within the nozzle, (2) the nozzle height, (3) the crater profile in one radial plane, and (4) the attenuation of several light beams due to flying particles ejected from the crater. The ambient (facility) pressure was read visually before and after each test.

Light-attenuation measurements.- The attenuation of a collimated beam of light due to ejecta was measured as a quantitative and objective indication of visibility impairment. The subjective effect of a given amount of light blockage is considered to be a subject for separate investigation. An attempt was made to locate two of the light beams so that they resembled the optical paths of a pilot's horizontal look and a downward look. A sketch of the setup is shown in figure 8. The two "pilot's" light beams passed through a position in space corresponding to the scaled window height above the nozzle exit plane. The lateral position of this fictitious window was not to scale, because the nozzle plenum chamber interfered. One of these pilot's light beams was directed horizontally, the other

was depressed approximately 36° below the horizontal. The light projectors and photo-cells for these attenuation measurements were attached to the nozzle plenum chamber and thus moved with the nozzle during its descent.

The attenuation of a third beam of light which was directed horizontally just above the surface of the bed was also measured on some of the tests. This beam passed through both sides of the cone of ejecta.

Crater profile measurements.- The depth of the particle bed in one radial plane was recorded as a function of time through the use of an X-ray system. An X-ray machine (150 kilovolts, 3 milliamperes, and self-rectified) was mounted above the bed of particles as shown in figure 3. The inverted-cone-shaped beam of X-rays from the machine passed through the bed of particles and impinged on the bedplate. This bedplate, 2.54 centimeters (1.0 inch) of steel and 1.9 centimeters (0.75 inch) of lead, had a 0.47-centimeter-wide (0.185-inch) slot which was located to be radial with respect to the axis of the nozzle. Beneath the bedplate, an X-ray film cassette mounted on a carriage traveled 4.32 cm/sec (1.7 in./sec) parallel to the bedplate and beneath the slot. The bed-plate attenuated the X-ray beam sufficiently to insure that for the total time of a run (1 to 10 seconds) the X-ray film was exposed significantly only to the X-rays which passed through the slot. A point on the film thus had coordinates of radial distance and time. The optical density of a point on the exposed and processed film was then a measure of the X-ray dosage during its passage under the slot and, therefore, the absorption of the particles above the slot. However, the density of a point on the film was governed by the absorption of particles along a slant line connecting the point on the film and the target of the X-ray tube. The method used to obtain the vertical bed depths is illustrated sub-sequently. Because of the great range of dosage received at the film plane as the bed eroded, especially if the erosion uncovered the bedplate, a double film arrangement was used. Two 35.6-centimeter (14-inch) by 43.2-centimeter (17-inch) sheets of high-speed X-ray film were used. One sheet was enclosed within two intensifying screens and one was laid on one screen. Thus, a double sensitivity system was achieved. Each point on a film traversed the slot in 0.11 second; thus, this time represents the best time resolution available. This overall system and the techniques were developed at Langley Research Center for the jet erosion experiments and are believed to be unique in using X-rays to obtain quantitative time-varying information.

TEST PROCEDURE

The procedure for conducting each test was essentially the same. Prior to the test, at atmospheric pressure, the particle bed was prepared, the dashpot mechanism was adjusted to obtain the test descent velocity, the X-ray film was loaded, and the light beams were adjusted. The vacuum cylinder was then closed and evacuated. When the

cylinder pressure reached test pressure, a pretest helium flow was started so that the jet stagnation pressure regulator could be adjusted to obtain the test thrust. This adjustment was made with the particle bed covered to prevent premature erosion of the bed. Once again, the cylinder pressure was lowered to test level at which time the particle-bed cover plate was removed. At this time also, the X-ray machine, film transport, and oscillograph were operated manually. Next, a program timer was started which automatically controlled helium flow (both start and stop), nozzle descent, and cameras. In most of the tests, the helium flow was still operating when the nozzle reached terminal height above the bed and continued to do so for several seconds before it was shut off; thus, a hover at the end of the descent was simulated.

X-RAY ANALYSIS

The general arrangement of the X-ray machine, particle bed, bedplate, and film are shown schematically in figure 9. Appendix C of reference 2 gives a general description of the X-ray—bed—film relations, but no details of the method of determining the crater shape from the processed X-ray film is given therein.

Because the intensity of the X-rays, like other forms of radiation, decreases inversely as the square of the distance from the source and the rays travel in straight lines, the surface of the undisturbed particle bed is not illuminated uniformly. Also, the intensity at the surface of the soil will decrease as the soil is eroded. The intensity of a ray at a point on the film plane is lower than the illumination at the surface because of the absorption of the X-rays by the particles along the slant line to the source. This absorption is an inverse exponential function of the length of the ray path through the particles. The relation between the optical density of a point on the processed film and a related soil bed depth is then a nonlinear relation and one which varies along the radial line being surveyed. The point-to-point variations, the nonlinear absorption, and the nonlinear film response were taken into account by the calibration method used. Calibration films were exposed with various depths of particles above the slot. These films yielded plots of optical density as a function of radial location for each of the particle depths used. A calibration was made for each type of particle that was used. The corrections from optical density (a measure of slant depth) to true depth were made graphically. A typical set of data that were obtained is shown in figure 10.

The optical density of the film was measured by a commercial instrument which surveyed a spot approximately 0.25 centimeter (0.1 inch) in diameter. A motor-driven scanning mechanism (light source, aperture, and photomultiplier tube) was constructed which traversed this survey spot across the film. The amplified output of the density-measuring instrument was recorded on a strip-chart recorder.

RESULTS AND DISCUSSION

Data are presented in figure 11 which show the erosion crater profiles at given times during each experiment. Test conditions were changed for each experiment and the conditions are listed. All dimensions are given in terms of the full-scale LM. Zero time is the start of the descent. Light-beam attenuation data that were obtained are presented in table I.

A motion-picture supplement L-1043 showing some of these tests has been prepared and is available on loan. A request card form and a description of the film are included at the back of this paper.

Erosion

The effects of thrust, descent velocity, particle size, and nozzle terminal height are illustrated in figures 12 to 19. Figures 12 to 15 show the change of crater depth with time at a radial station equal to two nozzle exit radii. The time range includes part of the nozzle descent and a constant nozzle height or hover condition which follows the descent. Figures 16 to 19 show the crater profiles that existed at the end of the descent for the same test.

Some difficulty was experienced in accurately repeating values for thrust, descent velocity, and nozzle terminal height. Therefore, it was not possible to isolate completely the effect of a single descent variable. In the comparisons of figures 12 to 19, average values are given for the descent conditions that were not deliberately varied.

Typical crater.- The stages of development of what is believed to be a typical crater are illustrated in figure 10. The small crater formed at first is shallow and relatively wide. A theoretical analysis (ref. 1) indicates that the erosion starts in a ring around the central stagnation point, the erosion starting at the radius where the free-stream dynamic pressure is a maximum. A central cone may exist at this time as indicated in the previous experiments reported in reference 2. This central cone is not measurable in these experiments because the low nozzle heights caused a blockage of the X-rays in this region. In the next phase of development, the crater deepens more rapidly than it spreads radially. As the depth of the crater approaches the depth of the bed, there is an apparent tendency for the vertical erosion rate to decrease as may be seen in figures 10 to 15. If erosion continues, both the top and bottom diameters increase and the walls become very steep. The maximum angle of the crater wall shown in figure 10, for instance, is approximately 55° as compared with a slump angle of 28° for the glass beads used.

Effect of descent conditions.- The effect of descent to various nozzle terminal heights is indicated in figures 12 and 16. These tests were made with an average thrust

of 27 800 N (6240 lb) and an average descent velocity of 1.17 m/sec (3.8 ft/sec). These data show that descents to lower terminal heights cause an increase in crater size. This effect is due to the fact that descents to lower heights result in longer times for erosion and the added time is at the low-altitude end of the descent where the exhaust jet causes the highest surface scrubbing velocity.

The effect of descent velocity is shown in figures 13 and 17. These tests were made with an average thrust of 28 100 N (6320 lb) to an average nozzle terminal height of 0.23 meter (0.7 foot). The penalty of a long erosion time due to a low descent speed is evident.

The importance of thrust magnitude on the erosion rate and the resulting crater size is illustrated in figures 14 and 18. These tests were made with an average descent speed of 1.38 m/sec (4.5 ft/sec) and terminated at an average nozzle height of 0.38 meter (1.2 feet).

These effects of thrust, descent speed, and nozzle terminal height on erosion rate and crater size indicate that a deliberate and cautious descent to the lunar surface will result in a larger crater than would the most abrupt descent that is structurally feasible. A high-velocity descent and a sudden high-thrust deceleration just before touchdown would also seem to be inadvisable because of crater enlargement. From an erosion standpoint, the best final approach would probably be a site inspection and selection maneuver at an altitude just above the incipient erosion height (see ref. 2) followed by a fast descent to the highest drop-in altitude that the structure can withstand.

Effect of particle size.- Figures 15 and 19 compare the erosion with two different particle sizes. These two tests were made with an average thrust of 29 500 N (6630 lb) at an average descent speed of 1.34 m/sec (4.4 ft/sec) and terminated at a nozzle height of 0.35 meter (1.1 feet). A much larger crater was eroded in the bed of large particles than in the bed of small particles. This effect (greater erosion of large particles than of small particles) has been discussed in references 1 and 2. It is important to remember that this effect holds true only for a range of particle sizes. If the particles are larger than some critical size (the size depending primarily on nozzle thrust and height), no erosion will occur because the aerodynamic lift and drag forces are insufficient to overcome the frictional restraint of an exposed particle and dislodge it. With very small particles (perhaps less than 20 micrometers), an additional restraint, interparticle attractive (or cohesion) force, becomes important and reduces the erosion below that for cohesionless particles. Thus, there is a "worst size" of particle from an erosion standpoint, and this size is just below the size for erosion cut-off. In the range of particle sizes between cohesion and erosion cut-off, the velocity of the ejected particle and the accompanying fallout distance decrease as the particle size increases.

12

Visibility

The visibility data gathered during the erosion experiments are given in table I. The values that are presented are the attenuation values in percent for each visibility station at the end of the nozzle descent. A value of 100 percent represents complete obstruction to the beam of light.

By reference to the description of the apparatus in figure 8, it can be seen that the inverted hollow cone of ejected material is intercepted at three different heights by the three light beams. The stationary horizontal light beam passes through the dust cone twice, parallel to and just above the surface of the bed. This beam suffers the most attenuation because the dust particles are close together and the light beam has to penetrate both sides of the dust cone. The next light beam location, representing the pilot's downward look, is attenuated less than the stationary horizontal beam; and the last light beam location, representing a pilot's horizontal look, is attenuated the least.

A comparison of the visibility data for experiments shown in figures 11(w) and 11(ee) for different particle sizes (0.13 cm (0.05 in.) and 2.54 cm (1.00 in.), respectively) shows that the light attenuations are approximately the same although the erosion rate was much higher for the large particle size. This comparison illustrates the fact that small particles will obstruct vision more effectively than large particles will, for an everyday example, consider fog and rain. Because absorption and reflection of the light beam are essentially surface phenomena of the material, a given mass of material dispersed as small particles in a light beam will attenuate the received beam more than the same mass of material dispersed as large particles. Thus, as pointed out by reference 1, there is some particle size which would result in the least visibility obstruction, since smaller sizes erode at a lower rate but obstruct light more, but larger particles will erode faster but obstruct light less.

Example Case Study

One of the experiments (fig. 11(e)) was selected as having descent parameters representative of what might be considered reasonable for a soft lander vehicle such as the lunar module. This experiment represented a thrust of 10 800 N (2420 lb) and a descent velocity of 0.61 m/sec (2.0 ft/sec) to a thrust cut-off height of 0.79 meter (2.6 feet). The soil particle size used for this experiment represented 2.54-centimeter (1.0-inch) particles, a size much greater than a cohesion-restrained size but much less than the largest size that could be eroded. The crater profile at thrust cut-off and the approximate locations of the nozzle exit and one foot of the vehicle at the thrust termination are shown in figure 20. The crater is approximately 0.76 meter (2.5 feet) deep and extends approximately halfway out to the foot. This crater results in the excavation of 6.20 cubic meters (219 cubic feet) of lunar surface material. A crater of this size might

not be hazardous in itself, but the consequence of this much outwardly ejected material on mission success is subject to speculation. If, as some of the photographs of Surveyor footprints indicate, the lunar surface material has some cohesion, the crater would be smaller than that shown here. If the landing mode included abrupt thrust increase just before thrust cut-off to eliminate excess descent speed, the resulting crater would be enlarged over the one illustrated.

It is important to note that the crater profile shown in figure 20 would occur precisely at thrust cut-off. Shortly after thrust cut-off (providing the soil material is noncohesive), a slumping of the crater would occur. This condition would tend to increase the diameter but decrease the depth of the crater. This effect is illustrated in figures 11(b) to 11(i). It should be noted also, that in the test for the configuration of figure 20, there was no degradation of visibility on the light beams simulating the pilot's horizontal or downward looks.

CONCLUSIONS

An experimental study has been made to investigate the lunar surface erosion and visibility effects that may be encountered during the lunar-module (LM) landing. The study was made by using a small cold flow nozzle in two large vacuum chambers with a simulated soil of glass beads or gravel. Some tentative conclusions have been reached from an examination of the data.

1. From an erosion and visibility standpoint, the best LM landing mode would involve a site inspection and selection above the incipient erosion height, and a fast descent to the highest drop-in altitude that the LM structure can withstand. Slower and more cautious descents with hovering just above touchdown would greatly increase the size of the crater.

2. For small size but noncohesive particles, light attenuation (and hence visibility attenuation) is considerable but the degree of erosion is probably not serious. Increasing particle size increases light transmission and erosion, maximum erosion occurring for particles only slightly smaller than the maximum size that could be dislodged. On the basis of theory and previously reported experiments, particles small enough to experience cohesive forces commensurate with their weight would probably erode at a much lower rate than noncohesive particles.

3. For landing conditions which might be representative of the lunar module mode with a thrust of approximately 11 100 N (2500 lb) at a descent speed of 0.61 m/sec (2.0 ft/sec), a thrust cut-off at a nozzle exit height of 0.76 meter (2.5 feet), and a soil composed of 2.54-centimeter (1.0-inch) rocks, the pilot's visibility will be good and the size of the crater would probably not be large enough to be troublesome. The crater at

14

thrust cut-off would be on the order of 0.76 meter (2.5 feet) deep, extend halfway out to the landing pads, and 6.20 cubic meters (219 cubic feet) of material would have been excavated. Subsequent to thrust cut-off, the crater would probably slump to a larger diameter, smaller depth configuration.

Langley Research Center,
  National Aeronautics and Space Administration,
    Langley Station, Hampton, Va., January 22, 1969,
      124-08-05-15-23.

REFERENCES

1. Roberts, Leonard: The Interaction of a Rocket Exhaust With the Lunar Surface. Presented at a Specialists' Meeting on "The Fluid Dynamic Aspects of Space Flight" (Marseille, France), AGARD, April 20-24, 1964.

2. Land, Norman S.; and Clark, Leonard V.: Experimental Investigation of Jet Impingement on Surfaces of Fine Particles in a Vacuum Environment. NASA TN D-2633, 1965.

3. Roberts, Leonard; and South, Jerry C., Jr.: Comments on Exhaust Flow Field and Surface Impingement. AIAA J., vol. 2, no. 5, May 1964, pp. 971-974.

4. Herdan, G.: Small Particle Statistics. Second ed., Academic Press, Inc., 1960.

5. Anon.: Standard Method of Test for Specific Gravity of Hydraulic Cement. ASTM Designation C 188-44. Pt. 4 of 1961 Supplement to Book of ASTM Standards Including Tentatives. Amer. Soc. Testing Mater., c.1961, pp. 190-191.

TABLE I.- TEST CONDITIONS AND LIGHT ATTENUATION MEASUREMENTS

[Dimensions are full scale]

Figure	Test	Condition								Attenuation of light beam, percent, for —		
		Thrust (a)		Descent velocity (b)		Nozzle terminal height		Particle size (c)		Horizontal look	Downward look	Stationary horizontal just above surface
		N	lb	m/sec	ft/sec	m	ft	cm	in.			
11(a)	1	30.4×10^3	6.84×10^3	4.24	13.9	0.82	2.7	0.41	0.16	42	78	----
11(b)	2	33.6	7.54	3.99	13.1	1.77	5.8	.41	.16	35	52	----
11(c)	6	11.6	2.61	.55	1.8	.79	2.6	1.14	.45	0	2	85
11(d)	7	8.1	1.83	.43	1.4	.70	2.3	.62	.24	0	0	44
11(e)	5	10.8	2.42	.61	2.0	.79	2.6	2.54	1.00	0	0	80
11(f)	9	10.8	2.42	.39	1.3	.67	2.2	9.40	3.7	0	6	92
11(g)	10	10.9	2.45	.61	2.0	.70	2.3	15.50	6.1	0	0	96
11(h)	4	11.6	2.61	1.89	6.2	.67	2.2	2.54	1.00	8	--	100
11(i)	3	29.3	6.59	3.38	11.1	1.43	4.7	2.54	1.00	9	29	----
11(j)	24	69.5	15.61	1.31	4.3	.46	1.5	1.96	.77	7	16	100
11(k)	25	100.5	22.58	1.32	4.3	.37	1.2	1.96	.77	23	67	89
11(l)	26	37.3	8.39	1.48	4.9	.43	1.4	1.96	.77	8	26	100
11(m)	35	27.3	6.13	1.06	3.5	.73	2.4	.97	.38	4	17	94
11(n)	37	27.2	6.11	1.23	4.1	.94	3.1	.97	.38	7	--	90
11(o)	38	27.6	6.20	1.31	4.3	1.34	4.4	.97	.38	6	13	78
11(p)	39	26.9	6.05	1.16	3.8	1.86	6.1	.97	.38	0	8	100
11(q)	28	41.3	9.29	1.21	4.0	.49	1.6	.97	.38	--	--	----
11(r)	29	26.4	5.93	2.30	7.6	.61	2.0	.97	.38	--	--	----
11(s)	31	26.4	5.93	4.10	13.3	.24	.8	.97	.38	10	14	92
11(t)	32	29.9	6.71	1.10	3.6	.21	.7	.97	.38	4	14	100
11(u)	8	11.7	2.64	.43	1.4	.76	2.5	.21	.08	0	4	100
11(v)	15	37.2	8.35	1.46	4.8	.27	.9	.13	.05	6	10	100
11(w)	16	28.7	6.45	1.29	4.2	.43	1.4	.13	.05	4	11	48
11(x)	19	30.4	6.84	2.14	7.0	.30	1.0	18.70	7.35	--	--	----
11(y)	46	45.0	10.11	1.42	4.7	.37	1.2	.97	.38	4	17	95
11(z)	47	21.2	4.77	1.39	4.5	.37	1.2	.97	.38	2	6	90
11(aa)	48	13.8	3.10	1.35	4.4	.37	1.2	.97	.38	4	6	90
11(bb)	49	89.5	20.12	1.36	4.5	.40	1.3	.97	.38	6	23	90
11(cc)	51	31.5	7.08	1.27	4.2	.34	1.1	2.54	1.00	8	8	100
11(dd)	52	59.1	13.29	1.31	4.3	.34	1.1	2.54	1.00	4	33	100
11(ee)	54	30.4	6.84	1.38	4.5	.27	.9	2.54	1.00	4	11	96
11(ff)	55	84.4	18.96	1.38	4.5	.30	1.0	2.54	1.00	22	50	100

[a]The conical nozzle was used for all tests except tests 1 and 2 which utilized the isentropic nozzle.

[b]All descents were constant velocities except those for tests 1 and 2 which were free. Descent velocity shown for tests 1 and 2 is at end of descent.

[c]All particles used for tests were glass beads except for tests 9 and 10 in which the particles were gravel.
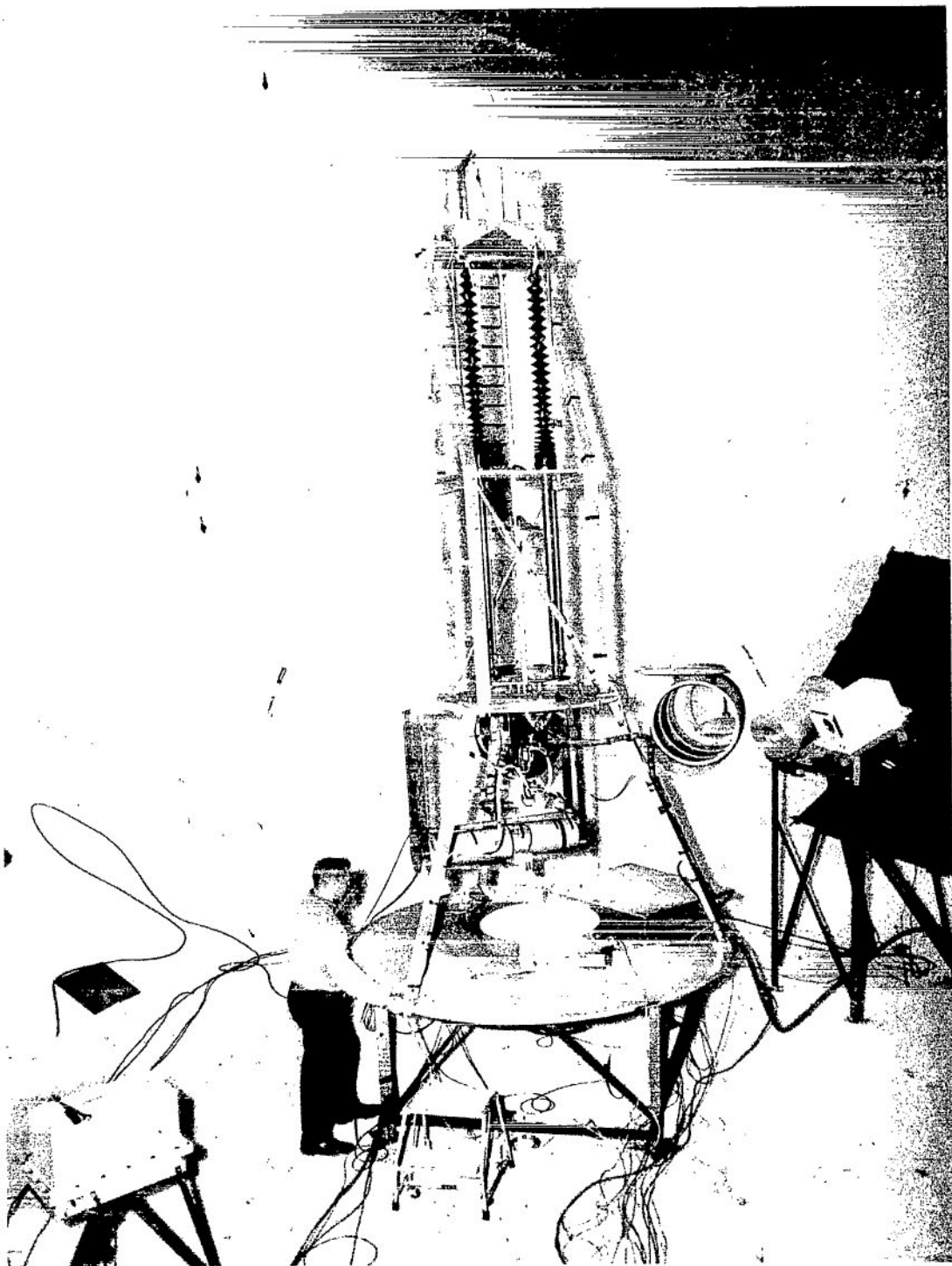
Figure 1.- Jet erosion apparatus in Langley 60-foot vacuum sphere   L-66-2354

Figure 2.- Jet erosion apparatus in the 55-foot vacuum cylinder at the Langley Research Center.   L-67-1783.1

18
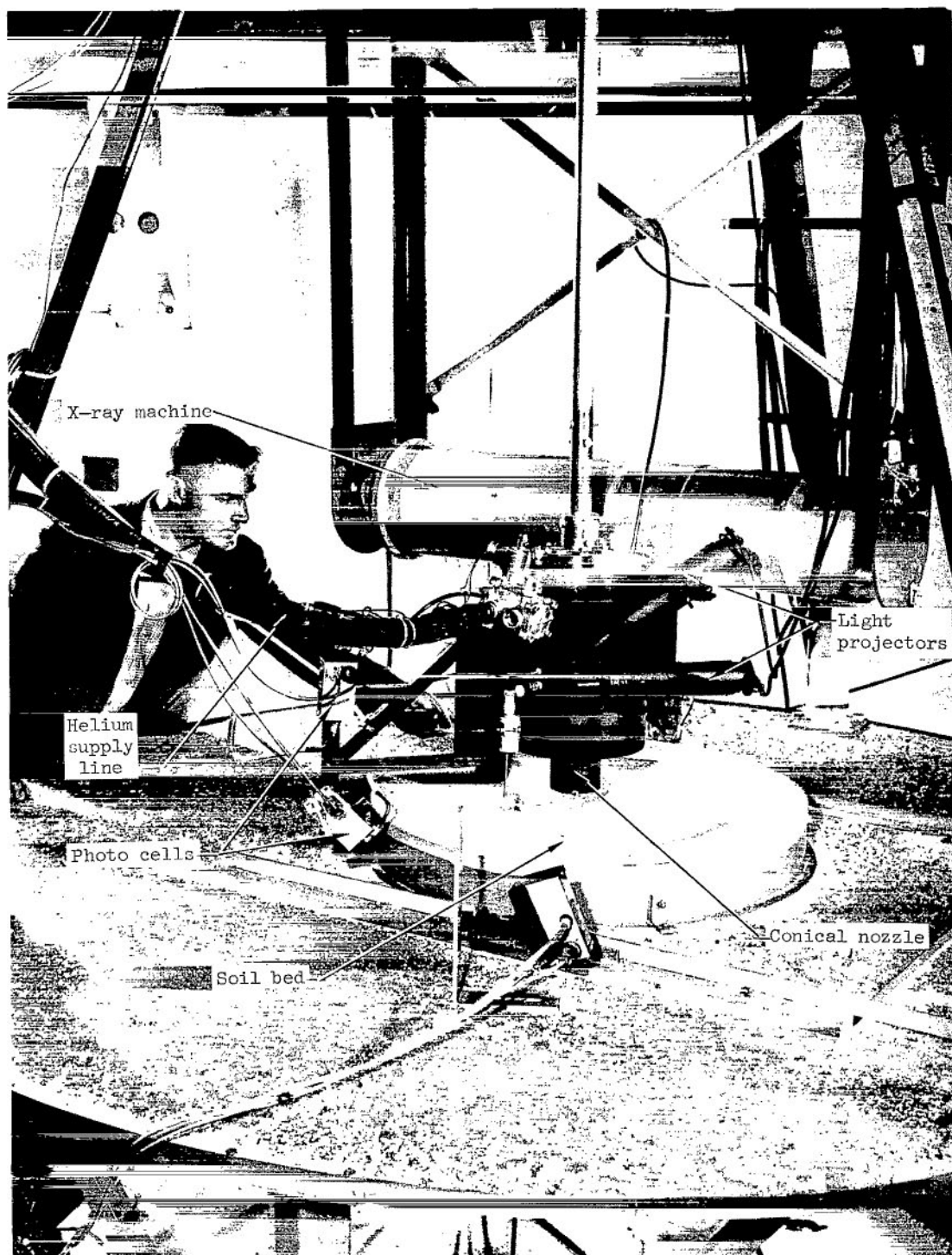
Figure 3.- Closeup of soil bed, X-ray machine, and nozzle.   L-67-1782.1
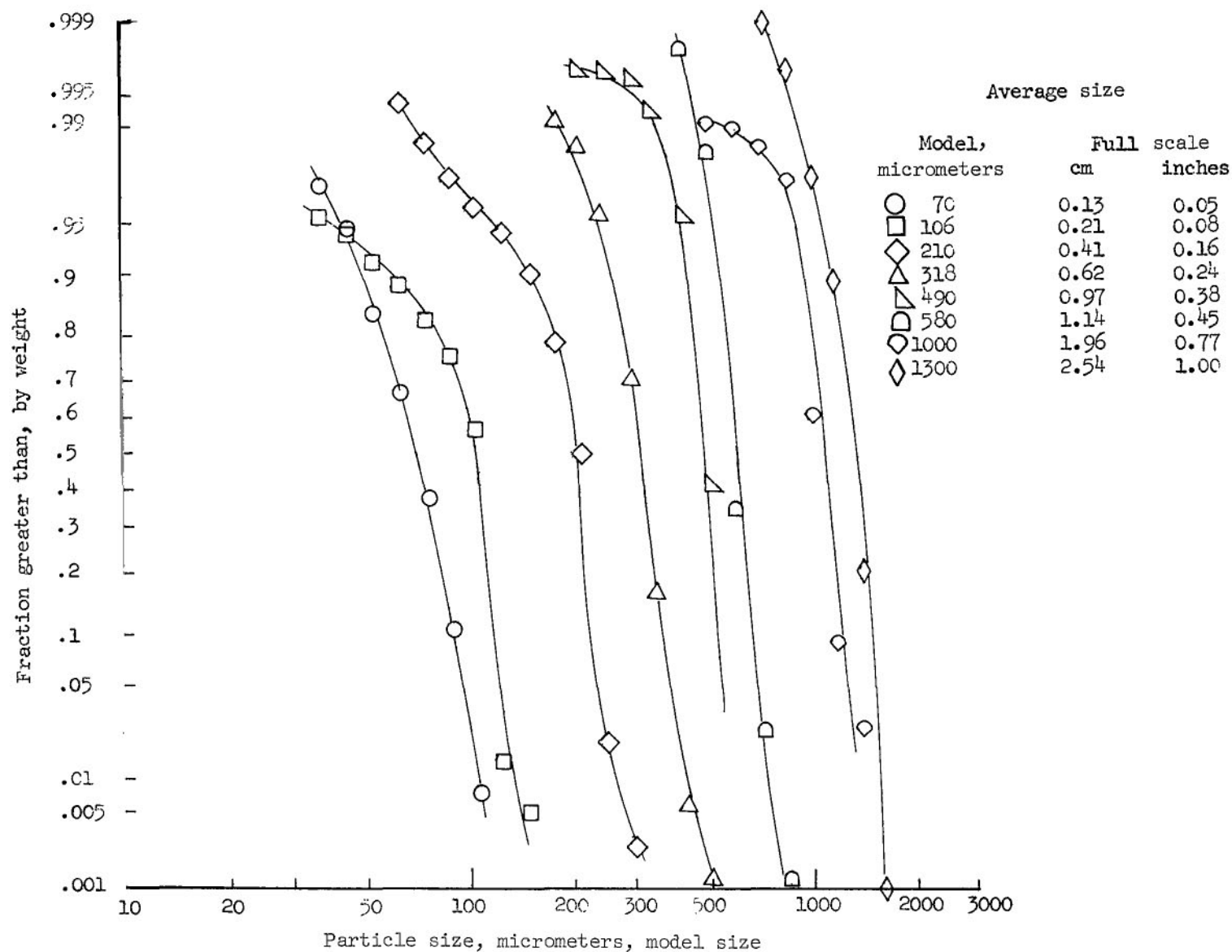
Figure 4.- Particle size distributions of glass beads used in tests.
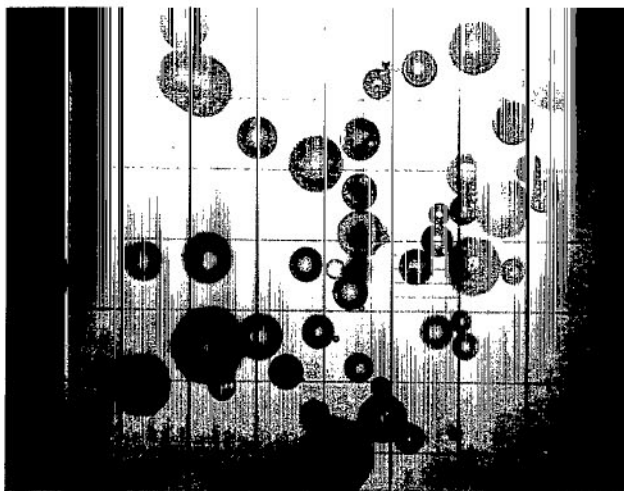
(a) Average particle size; 0.21 cm (0.08 in.).
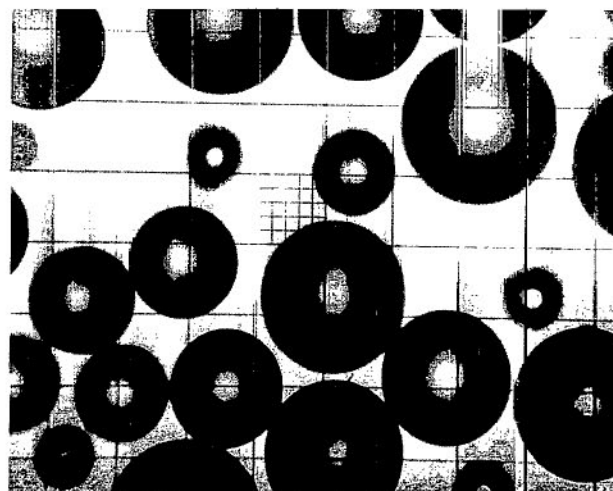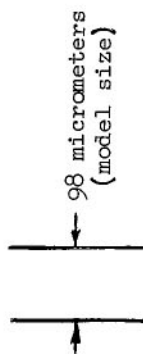
(b) Average particle size; 0.41 cm (0.16 in.).

98 micrometers (model size)

(c) Average particle size; 0.62 cm (0.24 in.).
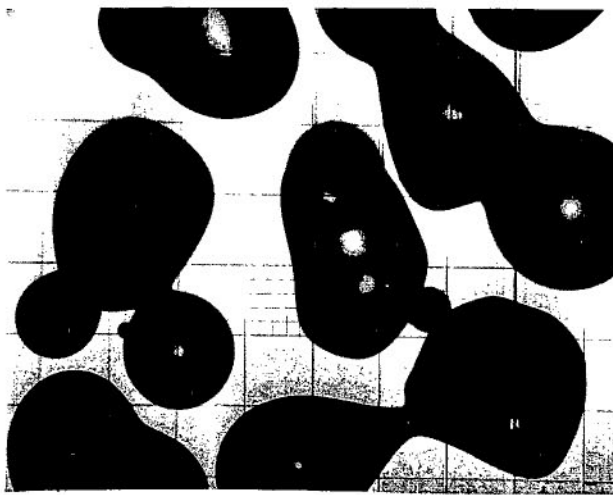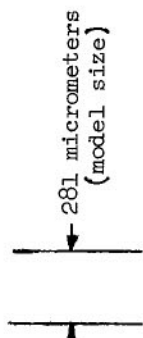
(d) Average particle size, 1.14 cm (0.45 in.).

281 micrometers (model size)

Figure 5.- Photographs of some typical particles.

L-69-1219

281 micrometers
(model size)
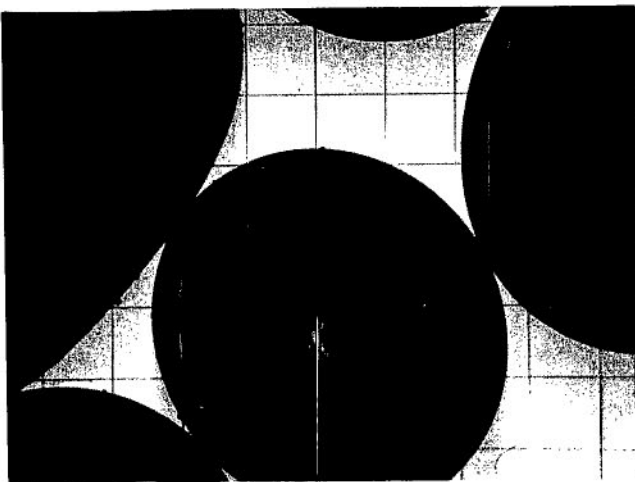
(e) Average particle size; 2.54 cm (1.00 in.).
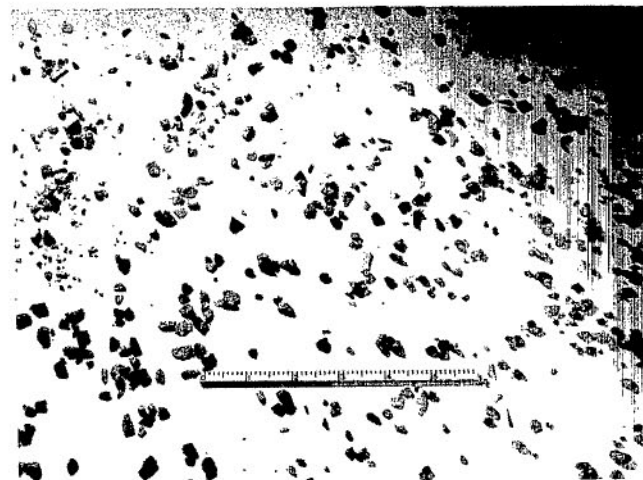
(f) Average particle size; 9.40 cm (3.7 in.).
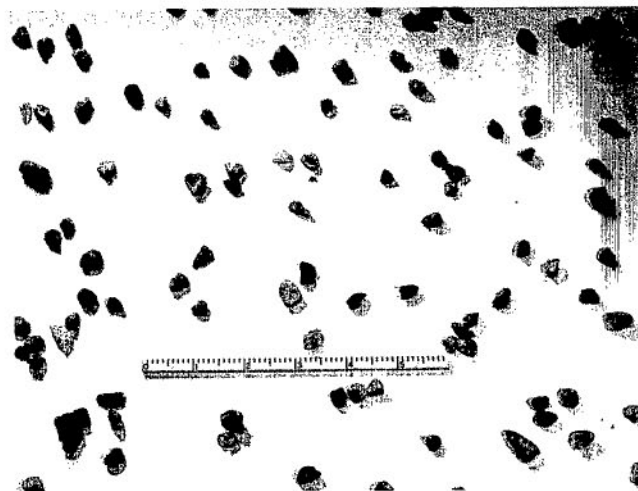
(g) Average particle size; 15.50 cm (6.1 in.).

Figure 5.- Concluded.

L-69-1220

Length from throat		Radius	
cm	in	cm	in
0	0	2.103	0.828
0.846	0.333	2.106	0.829
1.694	0.667	2.108	0.830
2.537	0.999	2.126	0.837
3.386	1.333	2.174	0.856
4.232	1.666	2.240	0.882
5.080	2.000	2.316	0.912
5.923	2.332	2.393	0.942
6.772	2.666	2.474	0.974
7.617	2.999	2.550	1.004
8.463	3.332	2.629	1.035
9.312	3.666	2.703	1.064
10.155	3.998	2.769	1.090
11.003	4.332	2.832	1.115
11.849	4.665	2.891	1.138
12.697	4.999	2.941	1.158
13.541	5.331	2.990	1.177
14.389	5.665	3.030	1.193
15.235	5.998	3.068	1.208
16.083	6.332	3.106	1.223
16.929	6.665	3.139	1.236
17.775	6.998	3.170	1.248
18.621	7.331	3.195	1.258
19.469	7.665	3.218	1.267
20.312	7.997	3.241	1.276
21.161	8.331	3.261	1.284
22.007	8.664	3.279	1.291
22.852	8.997	3.294	1.297
23.701	9.331	3.307	1.302
24.547	9.664	3.320	1.307
25.392	9.997	3.330	1.311
26.238	10.330	3.338	1.314
27.087	10.664	3.345	1.317
28.072	11.052	3.348	1.318
28.804	11.340	3.353	1.320
29.766	11.719	3.355	1.321
30.612	12.052	3.358	1.322
31.458	12.385	3.360	1.323
	Straight line		
42.321	16.662	3.378	1.330

Figure 6.- Isentropic axisymmetric nozzle. Dimensions are in cm (in.) model size.

23

Figure 7.- Conical axisymmetric nozzle and settling chamber. Dimensions are in cm (in.) model size.
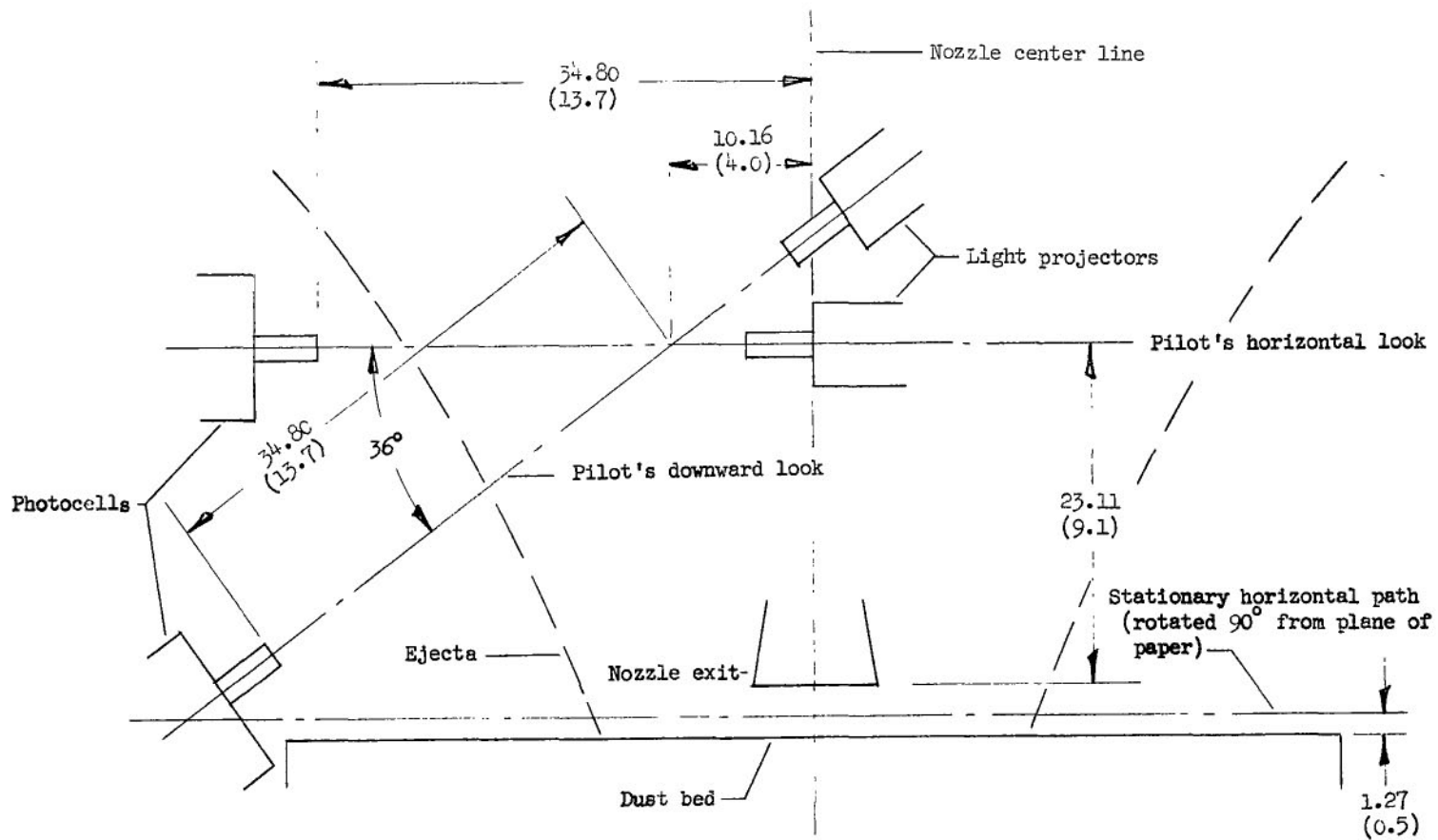
Figure 8.- Location of light paths for attenuation measurements. Plane of vehicle light paths 15.75 cm (6.2 in.) from center line of nozzle. Dimensions are in cm (in.) model size.
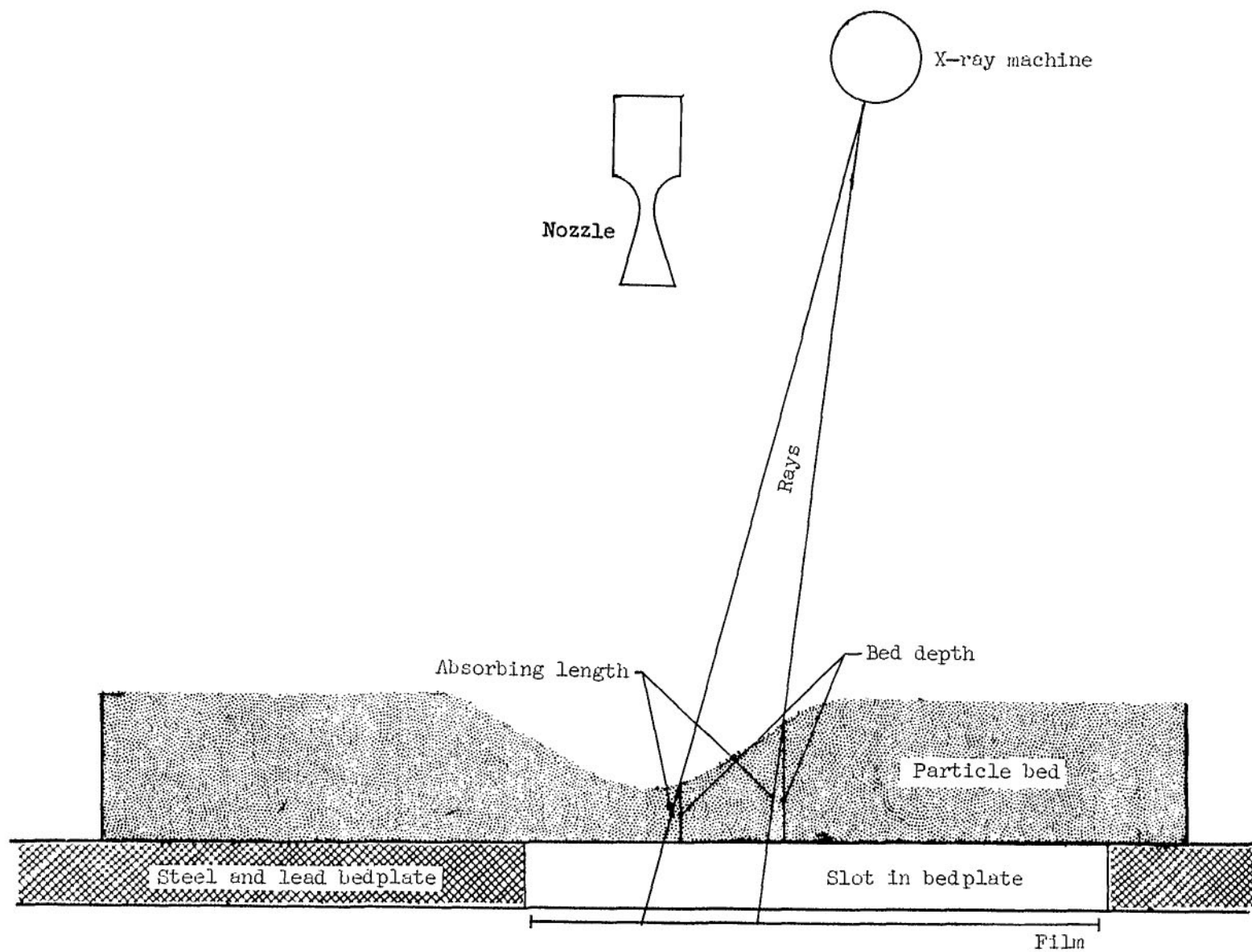
Figure 9.- Schematic of X-ray—bed—film arrangement.
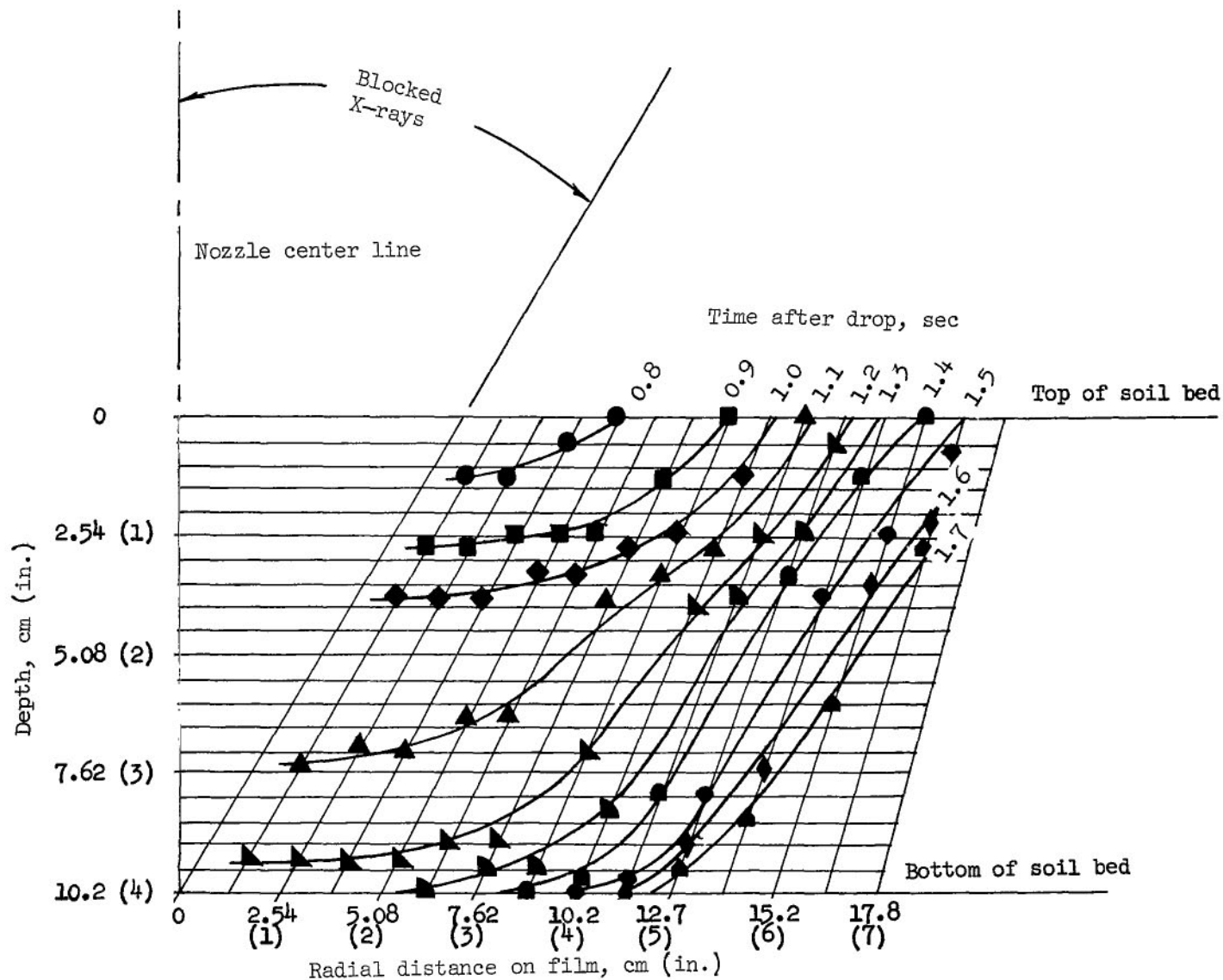
Figure 10.- Typical crater data obtained from an X-ray film made during a test. Correction grid shown; times and lengths shown are model size.
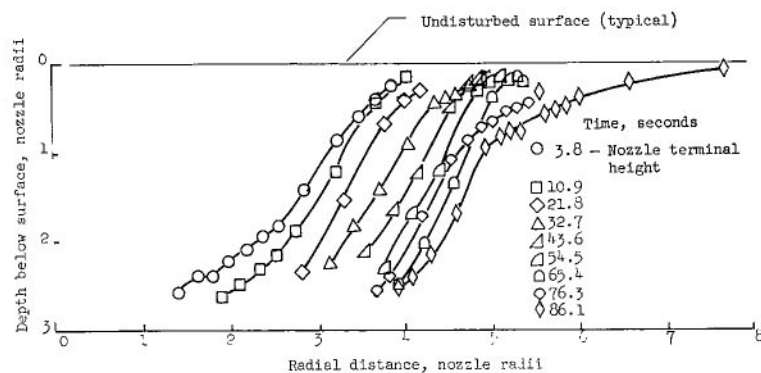
(a) Free descent with isentropic nozzle. Velocity at nozzle terminal height, 4.24 m/sec (13.9 ft/sec); thrust, 30 400 N (6840 lb); nozzle terminal height, 0.82 m (2.7 ft); 0.41 cm (0.16 in.) glass-bead particles.
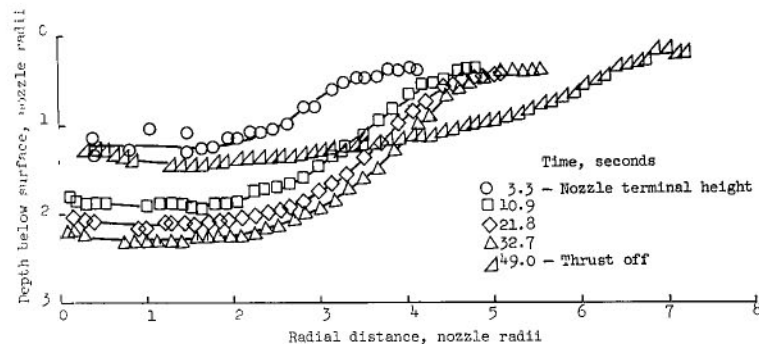
(b) Free descent with isentropic nozzle. Velocity at nozzle terminal height, 3.99 m/sec (13.1 ft/sec); thrust, 33 600 N (7540 lb); nozzle terminal height, 1.77 m (5.8 ft); 0.41 cm (0.16 in.) glass-bead particles.
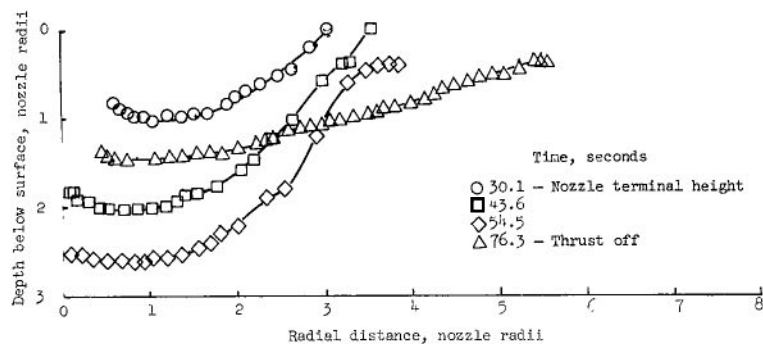
(c) Descent velocity, 0.55 m/sec (1.8 ft/sec) with conical nozzle; thrust, 11 600 N (2610 lb); nozzle terminal height, 0.79 m (2.6 ft); 1.14 cm (0.45 in.) glass-bead particles.
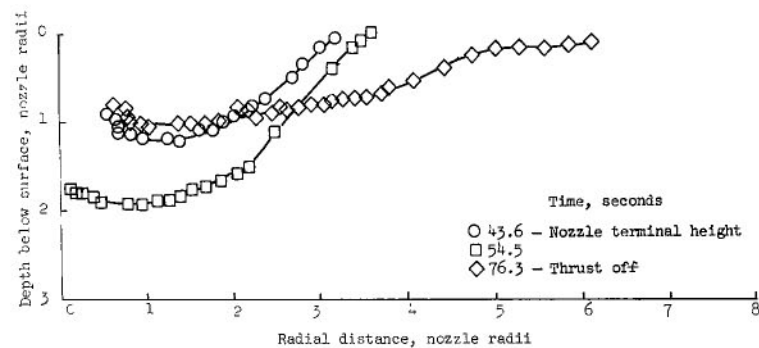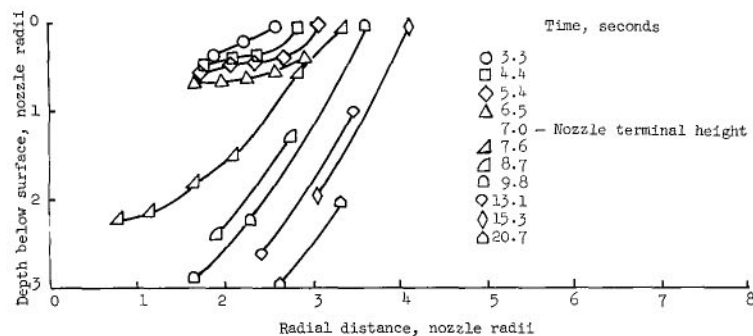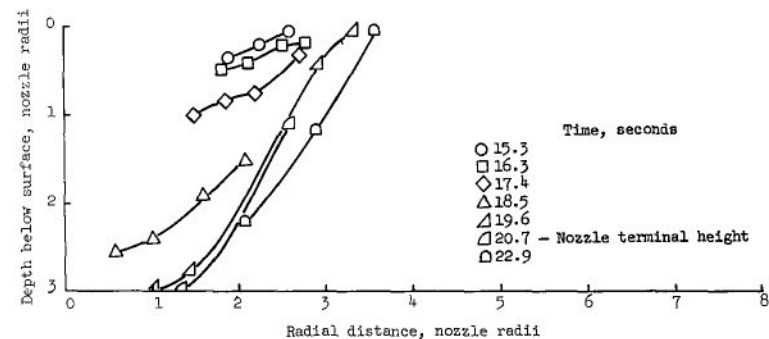
(d) Descent velocity, 0.43 m/sec (1.4 ft/sec) with conical nozzle; thrust, 8140 N (1830 lb); nozzle terminal height, 0.70 m (2.3 ft); 0.62 cm (0.24 in.) glass-bead particles.

Figure 11.- Erosion crater profiles. (Full scale.)
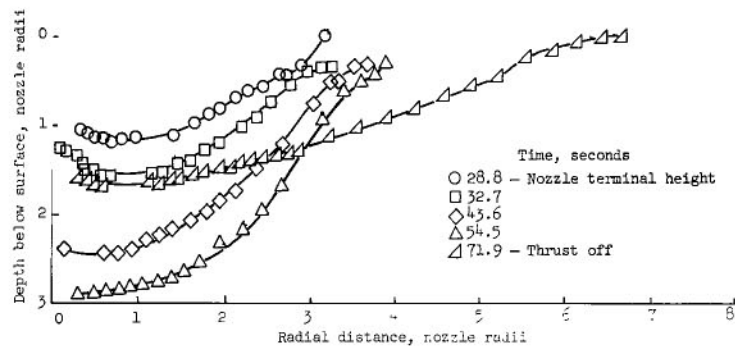
(e) Descent velocity, 0.61 m/sec (2.0 ft/sec) with conical nozzle; thrust, 10 800 N (2420 lb); nozzle terminal height, 0.79 m (2.6 ft); 2.54 cm (1.00 in.) glass-bead particles.
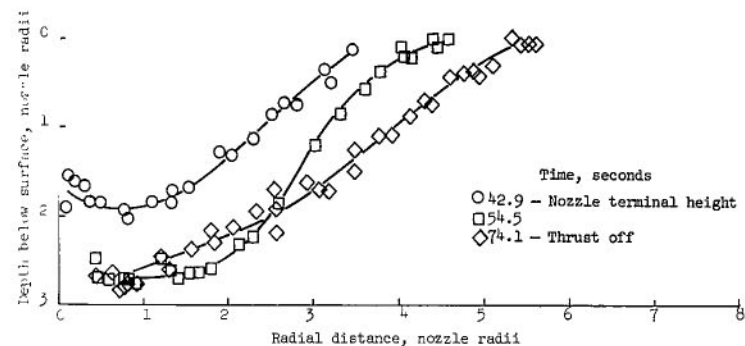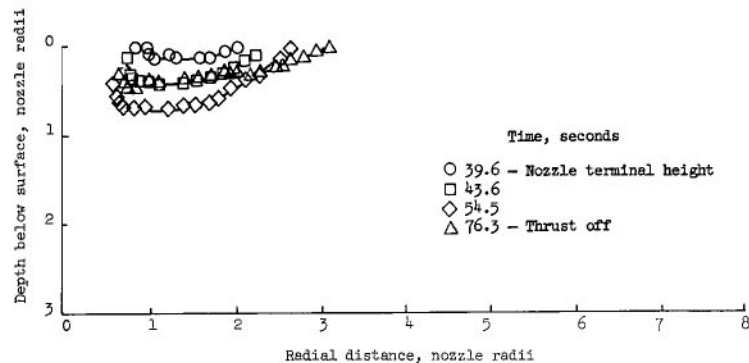
(f) Descent velocity, 0.39 m/sec (1.3 ft/sec) with conical nozzle; thrust, 10 800 N (2420 lb); nozzle terminal height, 0.67 m (2.2 ft); 9.40 cm (3.7 in.) gravel.
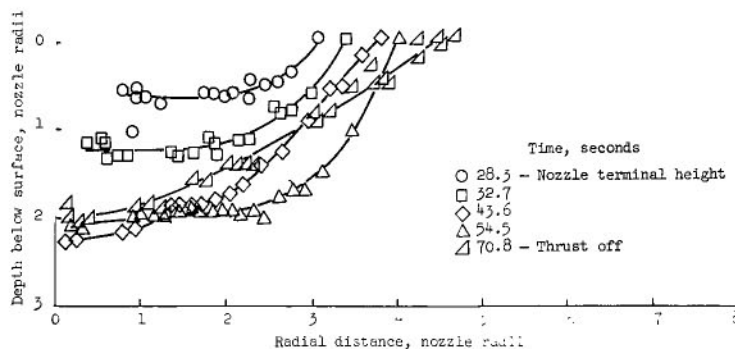
(g) Descent velocity, 0.61 m/sec (2.0 ft/sec) with conical nozzle; thrust, 10 900 N (2450 lb); nozzle terminal height, 0.70 m (2.3 ft); 15.50 cm (6.1 in.) gravel.
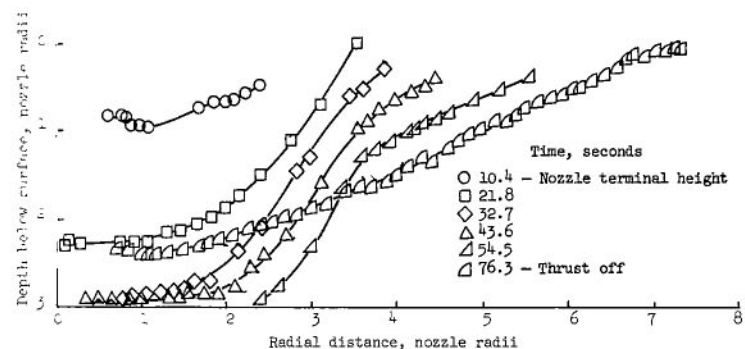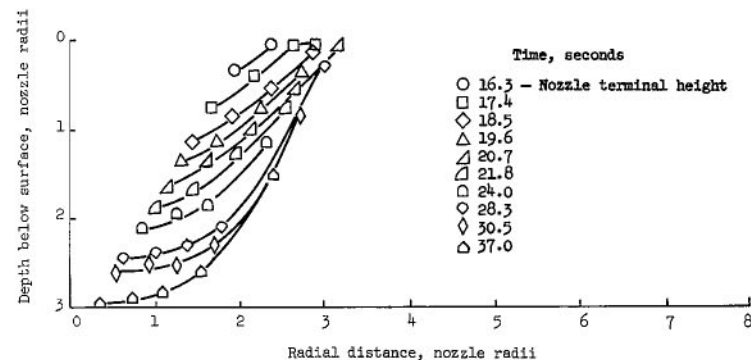
(h) Descent velocity, 1.89 m/sec (6.2 ft/sec) with conical nozzle; thrust, 11 600 N (2610 lb); nozzle terminal height, 0.67 m (2.2 ft); 2.54 cm (1.00 in.) glass-bead particles.
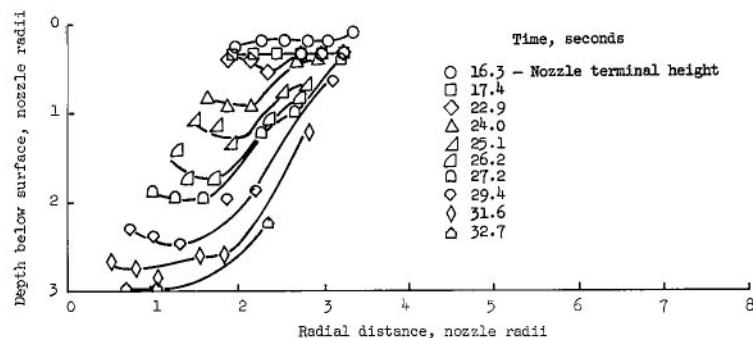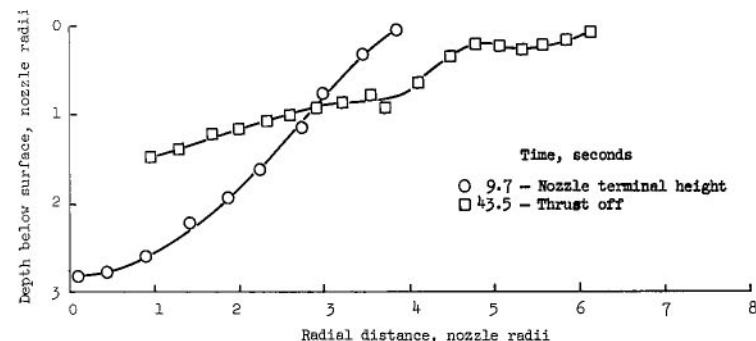
Figure 11.- Continued.
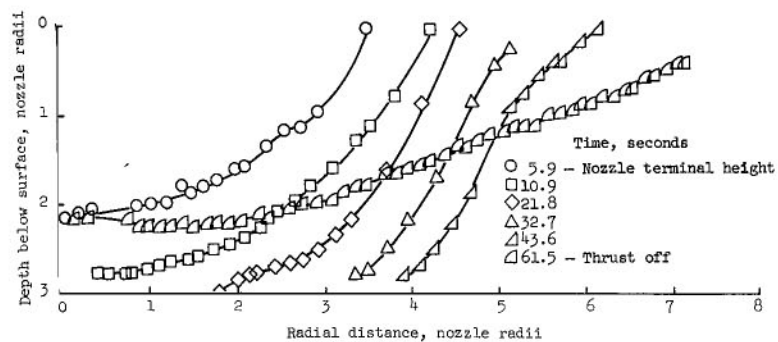
(i) Descent velocity, 3.38 m/sec (11.1 ft/sec) with conical nozzle; thrust, 29 300 N (6590 lb); nozzle terminal height, 1.43 m (4.7 ft); 2.54 cm (1.00 in.) glass-bead particles.
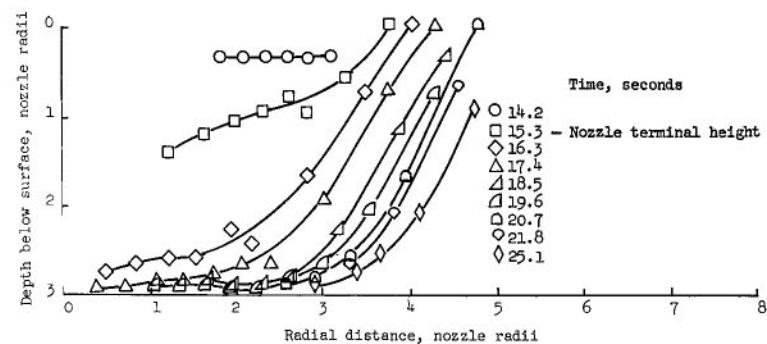
(j) Descent velocity, 1.31 m/sec (4.3 ft/sec) with conical nozzle; thrust, 69 500 N (15 610 lb); nozzle terminal height, 0.46 m (1.5 ft); 1.96 cm (0.77 in.) glass-bead particles.
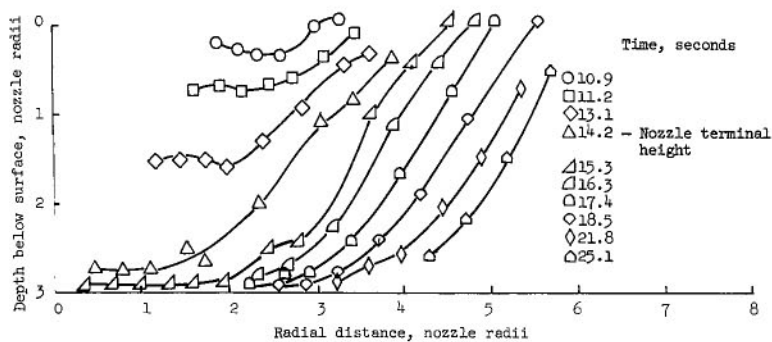
(k) Descent velocity, 1.32 m/sec (4.3 ft/sec) with conical nozzle; thrust, 100 500 N (22 580 lb); nozzle terminal height, 0.37 m (1.2 ft); 1.96 cm (0.77 in.) glass-bead particles.
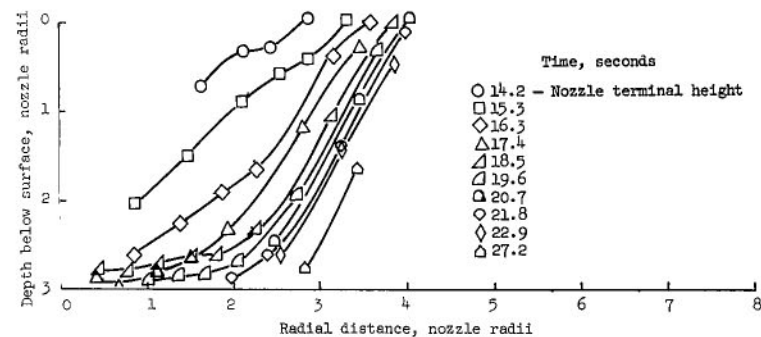
(l) Descent velocity, 1.48 m/sec (4.9 ft/sec) with conical nozzle; thrust, 37 300 N (8390 lb); nozzle terminal height, 0.43 m (1.4 ft); 1.96 cm (0.77 in.) glass-bead particles.
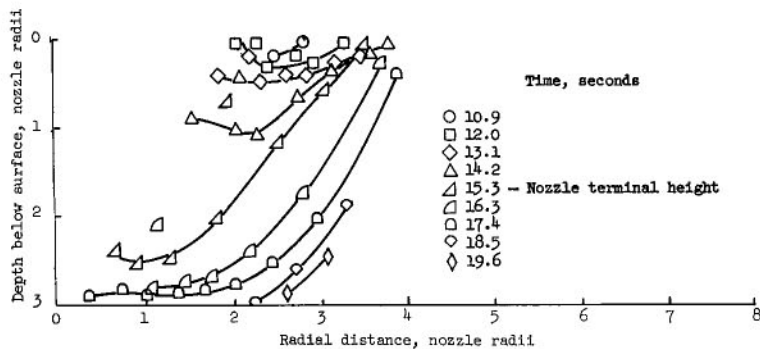
Figure 11.- Continued.
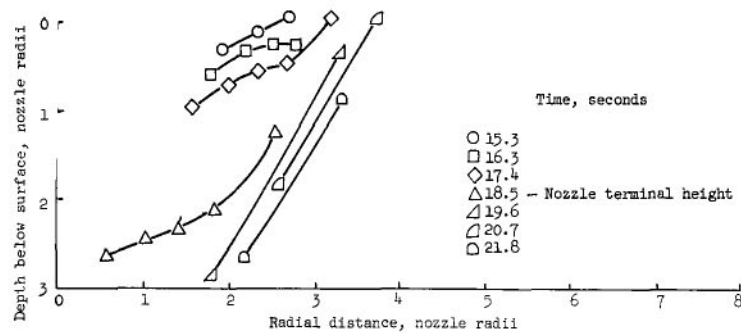
(m) Descent velocity, 1.06 m/sec (3.5 ft/sec) with conical nozzle; thrust, 27 300 N (6130 lb); nozzle terminal height, 0.73 m (2.4 ft); 0.97 cm (0.38 in.) glass-bead particles.
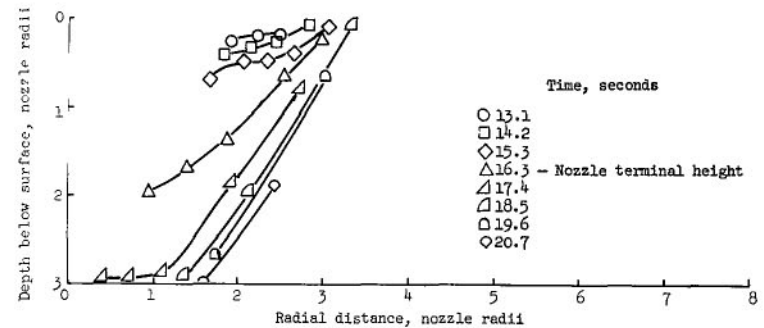
(n) Descent velocity, 1.23 m/sec (4.1 ft/sec) with conical nozzle; thrust, 27 200 N (6110 lb); nozzle terminal height, 0.94 m (3.1 ft); 0.97 cm (0.38 in.) glass-bead particles.
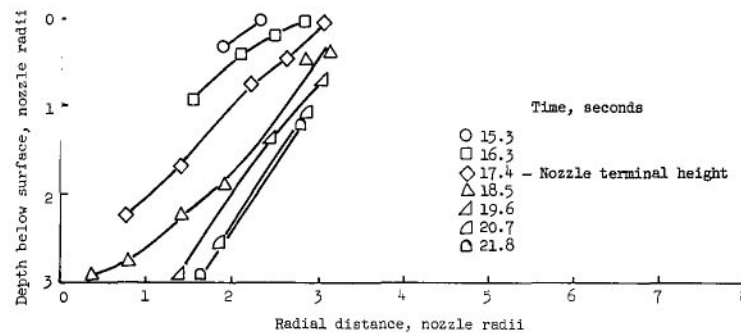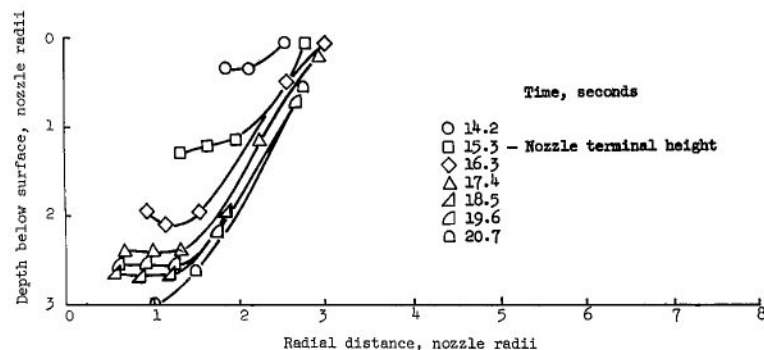
(o) Descent velocity, 1.31 m/sec (4.3 ft/sec) with conical nozzle; thrust, 27 600 N (6200 lb); nozzle terminal height, 1.34 m (4.4 ft); 0.97 cm (0.38 in.) glass-bead particles.
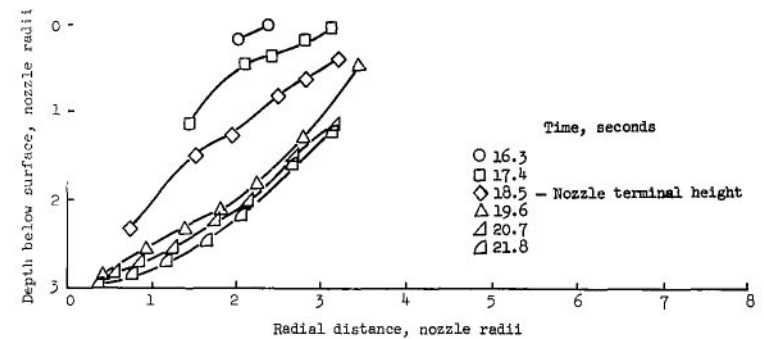
(p) Descent velocity, 1.16 m/sec (3.8 ft/sec) with conical nozzle; thrust, 26 900 N (6050 lb); nozzle terminal height, 1.86 m (6.1 ft); 0.97 cm (0.38 in.) glass-bead particles.
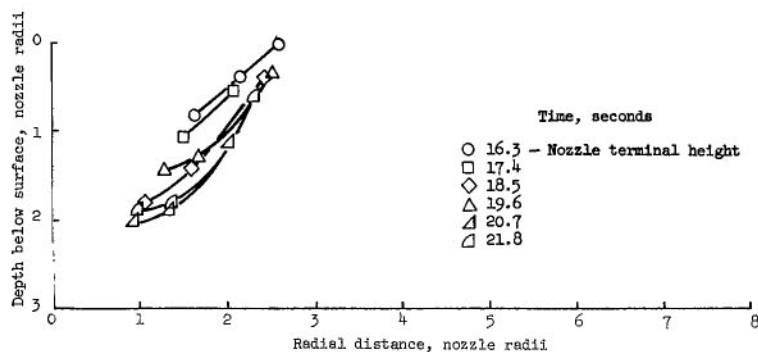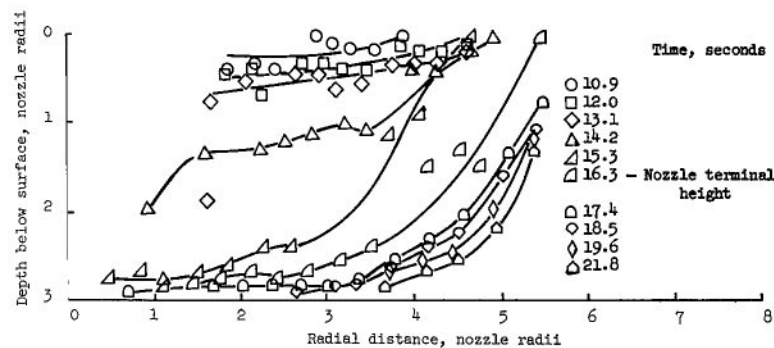
Figure 11.- Continued.
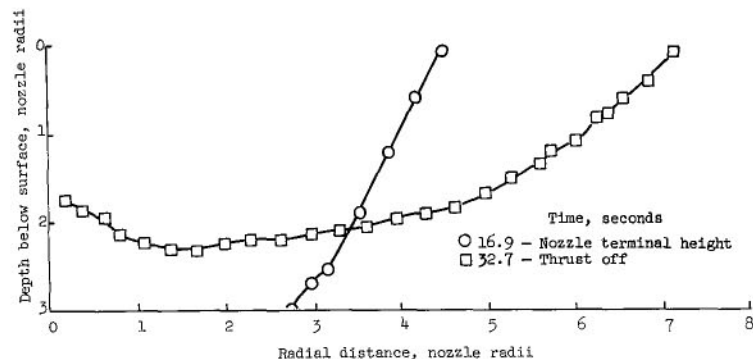
(q) Descent velocity, 1.21 m/sec (4.0 ft/sec) with conical nozzle; thrust, 41 300 N (9290 lb); nozzle terminal height, 0.49 m (1.6 ft); 0.97 cm (0.38 in.) glass-bead particles.
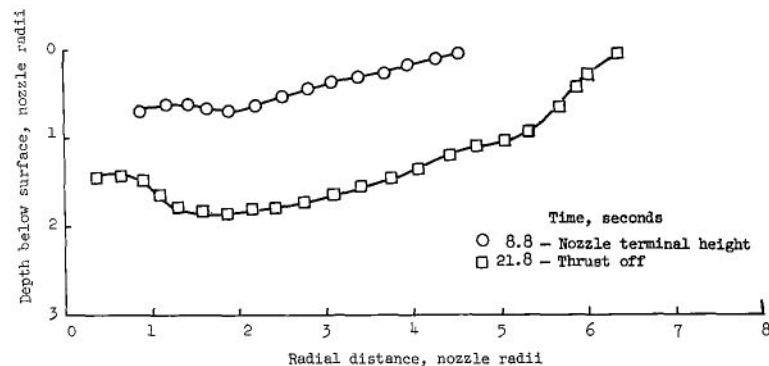
(r) Descent velocity, 2.30 m/sec (7.6 ft/sec) with conical nozzle; thrust, 26 400 N (5930 lb); nozzle terminal height, 0.61 m (2.0 ft); 0.97 cm (0.38 in.) glass-bead particles.
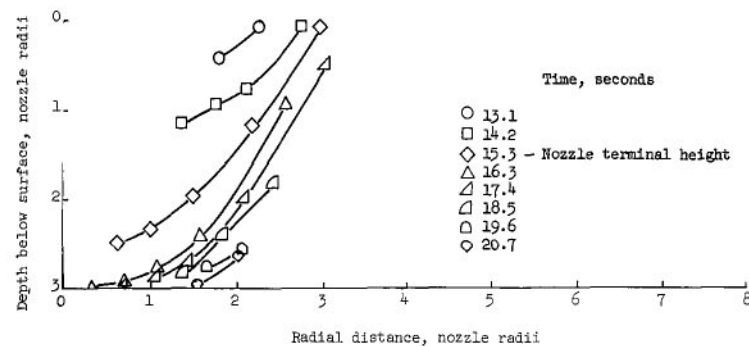
(s) Descent velocity, 4.10 m/sec (13.3 ft/sec) with conical nozzle; thrust, 26 400 N (5930 lb); nozzle terminal height, 0.24 m (0.8 ft); 0.97 cm (0.38 in.) glass-bead particles.

(t) Descent velocity, 1.10 m/sec (3.6 ft/sec) with conical nozzle; thrust, 29 900 N (6710 lb); nozzle terminal height, 0.21 m (0.7 ft); 0.97 cm (0.38 in.) glass-bead particles.

Figure 11.- Continued.

(u) Descent velocity, 0.43 m/sec (1.4 ft/sec) with conical nozzle; thrust, 11 700 N (2640 lb); nozzle terminal height, 0.76 m (2.5 ft); 0.21 cm (0.08 in.) glass-bead particles.

(v) Descent velocity, 1.46 m/sec (4.8 ft/sec) with conical nozzle; thrust, 37 200 N (8350 lb); nozzle terminal height, 0.27 m (0.9 ft); 0.13 cm (0.05 in.) glass-bead particles.

(w) Descent velocity, 1.29 m/sec (4.2 ft/sec) with conical nozzle; thrust, 28 700 N (6450 lb); nozzle terminal height, 0.43 m (1.4 ft); 0.13 cm (0.05 in.) glass-bead particles.
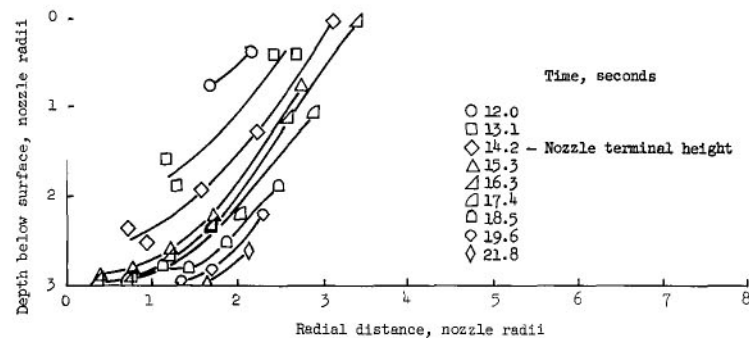
(x) Descent velocity, 2.14 m/sec (7.0 ft/sec) with conical nozzle; thrust, 30 400 N (6840 lb); nozzle terminal height, 0.30 m (1.0 ft); 18.70 cm (7.35 in.) glass-bead particles.

Figure 11.- Continued.

(y) Descent velocity, 1.42 m/sec (4.7 ft/sec) with conical nozzle; thrust, 45 000 N (10 110 lb); nozzle terminal height, 0.37 m (1.2 ft); 0.97 cm (0.38 in.) glass-bead particles.

(z) Descent velocity, 1.39 m/sec (4.5 ft/sec) with conical nozzle; thrust, 21 200 N (4770 lb); nozzle terminal height, 0.37 m (1.2 ft); 0.97 cm (0.38 in.) glass-bead particles.

(aa) Descent velocity, 1.35 m/sec (4.4 ft/sec) with conical nozzle; thrust, 13 800 N (3100 lb); nozzle terminal height, 0.37 m (1.2 ft); 0.97 cm (0.38 in.) glass-bead particles.

(bb) Descent velocity, 1.36 m/sec (4.5 ft/sec) with conical nozzle; thrust, 89 500 N (20 120 lb); nozzle terminal height, 0.40 m (1.3 ft); 0.97 cm (0.38 in.) glass-bead particles.

Figure 11.- Continued.

(cc) Descent velocity, 1.27 m/sec (4.2 ft/sec) with conical nozzle; thrust, 31 500 N (7080 lb); nozzle terminal height, 0.34 m (1.1 ft); 2.54 cm (1.00 in.) glass-bead particles.
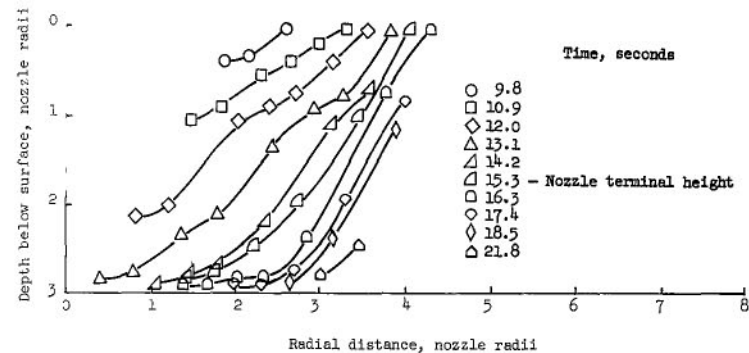
(dd) Descent velocity, 1.31 m/sec (4.3 ft/sec) with conical nozzle; thrust, 59 100 N (13 290 lb); nozzle terminal height, 0.34 m (1.1 ft); 2.54 cm (1.00 in.) glass-bead particles.

(ee) Descent velocity, 1.38 m/sec (4.5 ft/sec) with conical nozzle; thrust, 30 400 N (6840 lb); nozzle terminal height, 0.27 m (0.9 ft); 2.54 cm (1.00 in.) glass-bead particles.
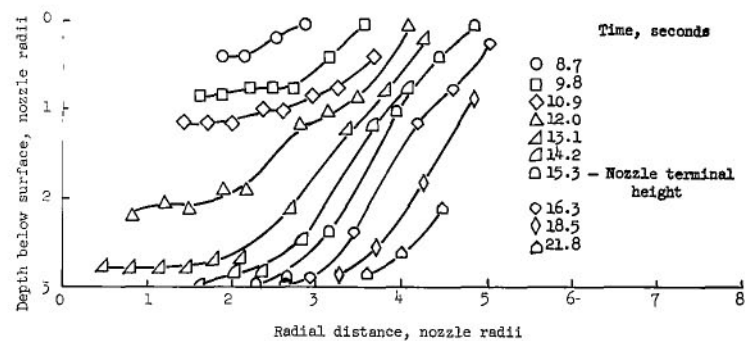
(ff) Descent velocity, 1.38 m/sec (4.5 ft/sec) with conical nozzle; thrust, 84 400 N (18 960 lb); nozzle terminal height, 0.30 m (1.0 ft); 2.54 cm (1.00 in.) glass-bead particles.

Figure 11.- Concluded.
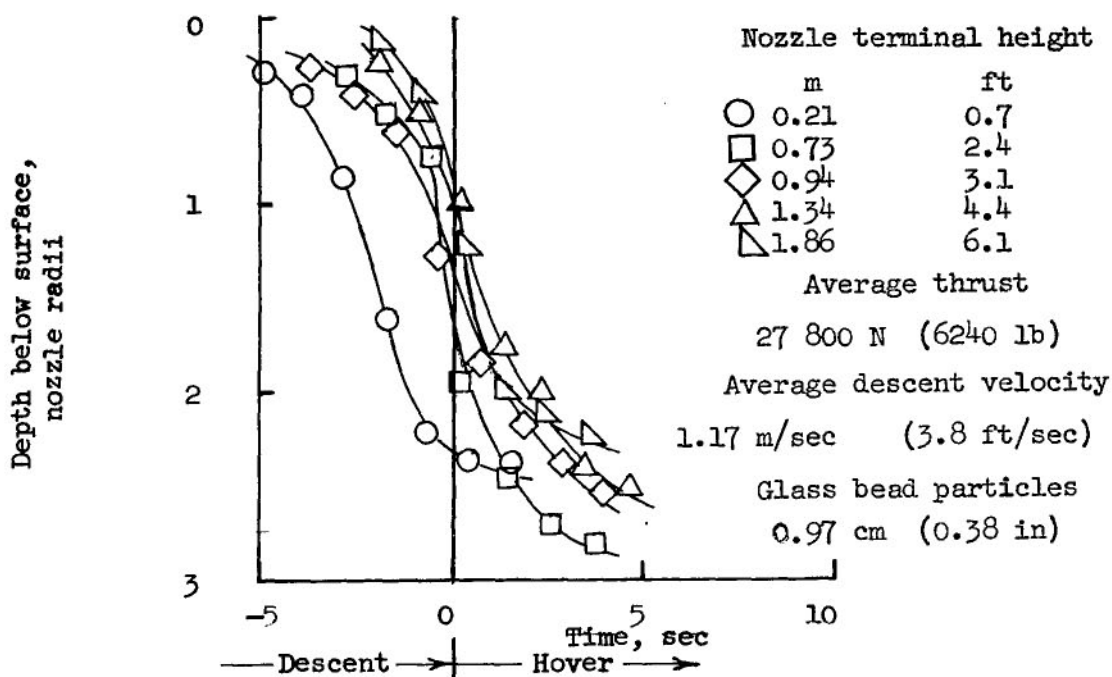
Figure 12.- Effect of nozzle terminal height on crater depth at a radial distance from center line equal to two nozzle radii.
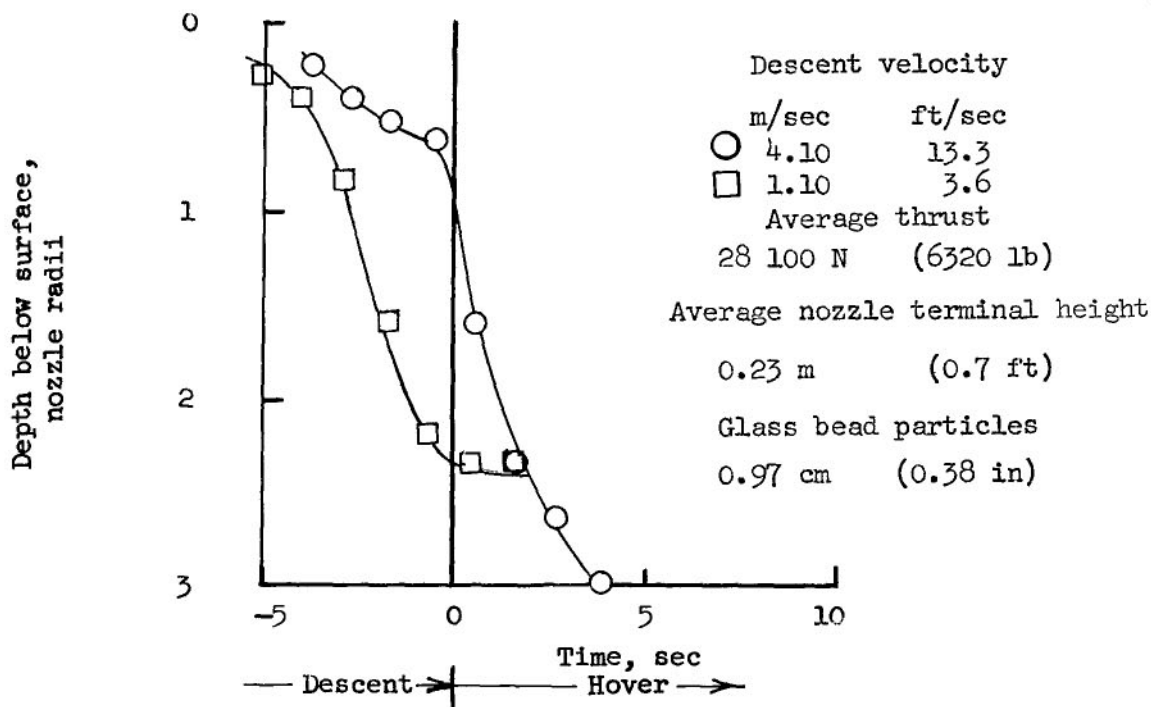
Figure 13.- Effect of descent velocity on crater depth at a radial distance from center line equal to two nozzle radii.
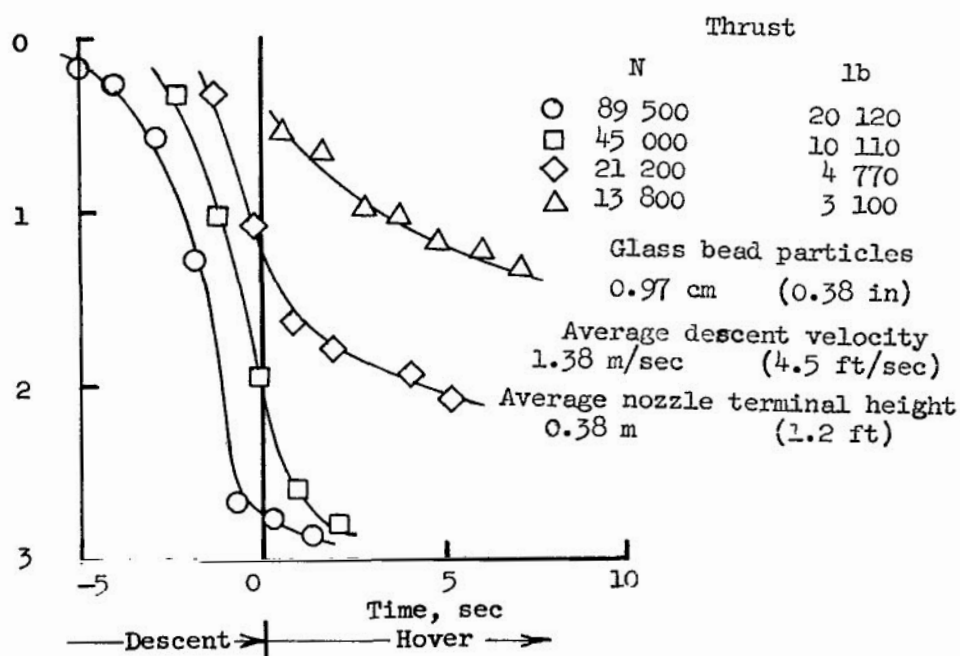
Figure 14.- Effect of thrust on crater depth at a radial distance from center line equal to two nozzle radii.
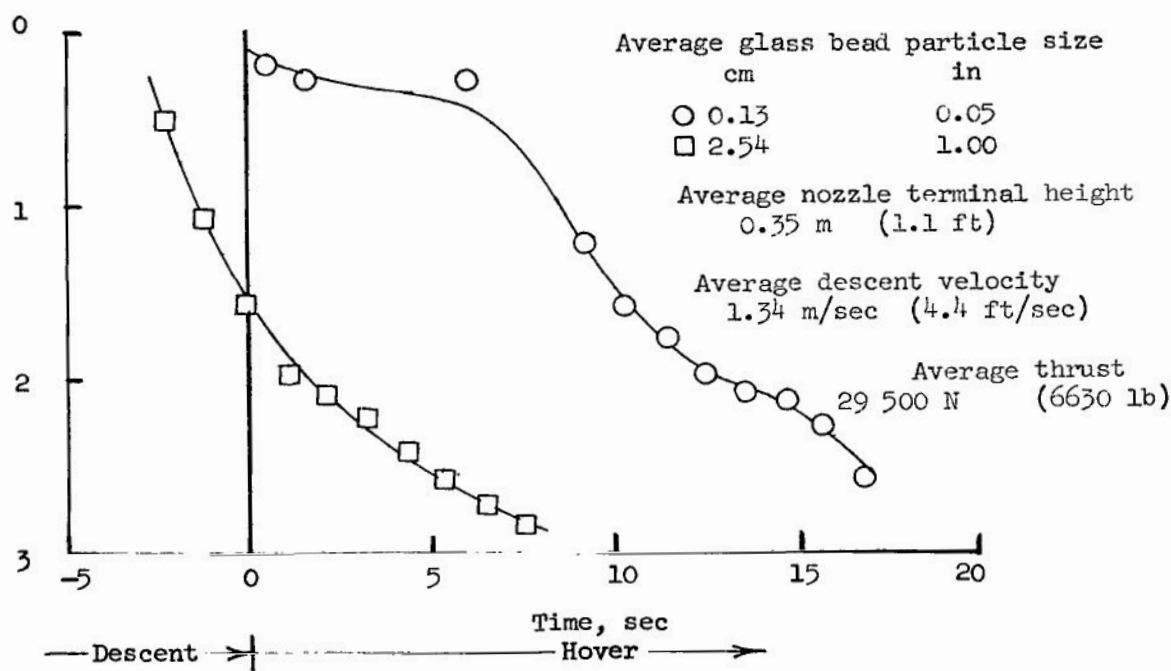

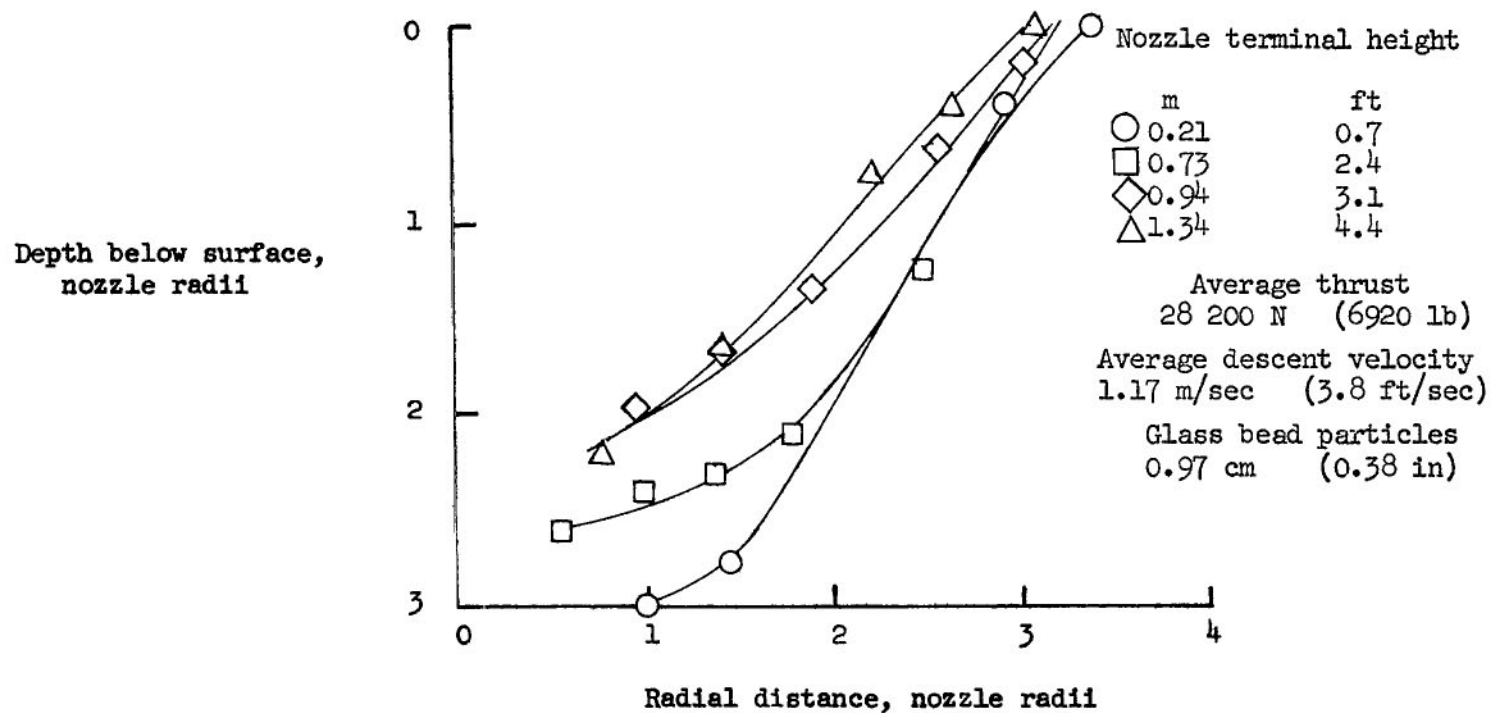Figure 15.- Effect of particle size on crater depth at a radial distance from center line equal to two nozzle radii.

37

Figure 16.- Effect of nozzle terminal height on crater profile at end of descent.
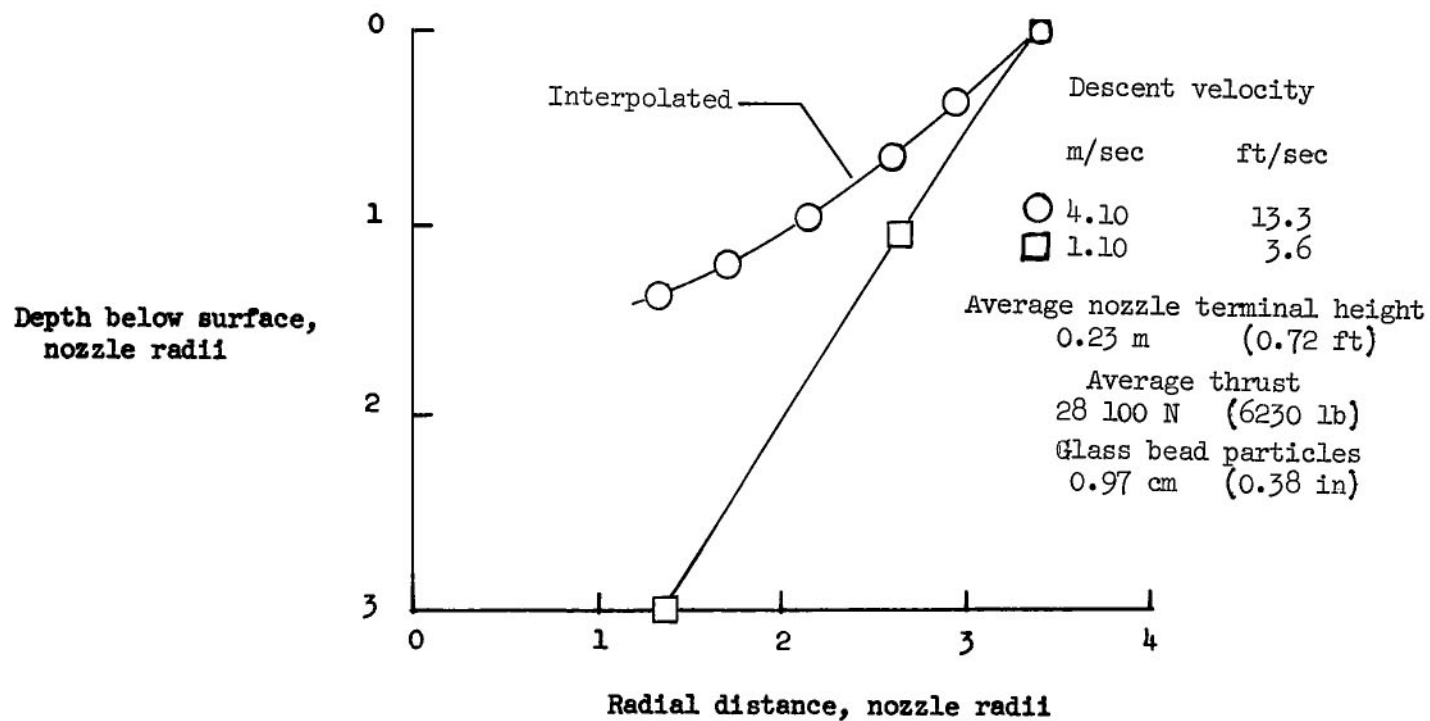
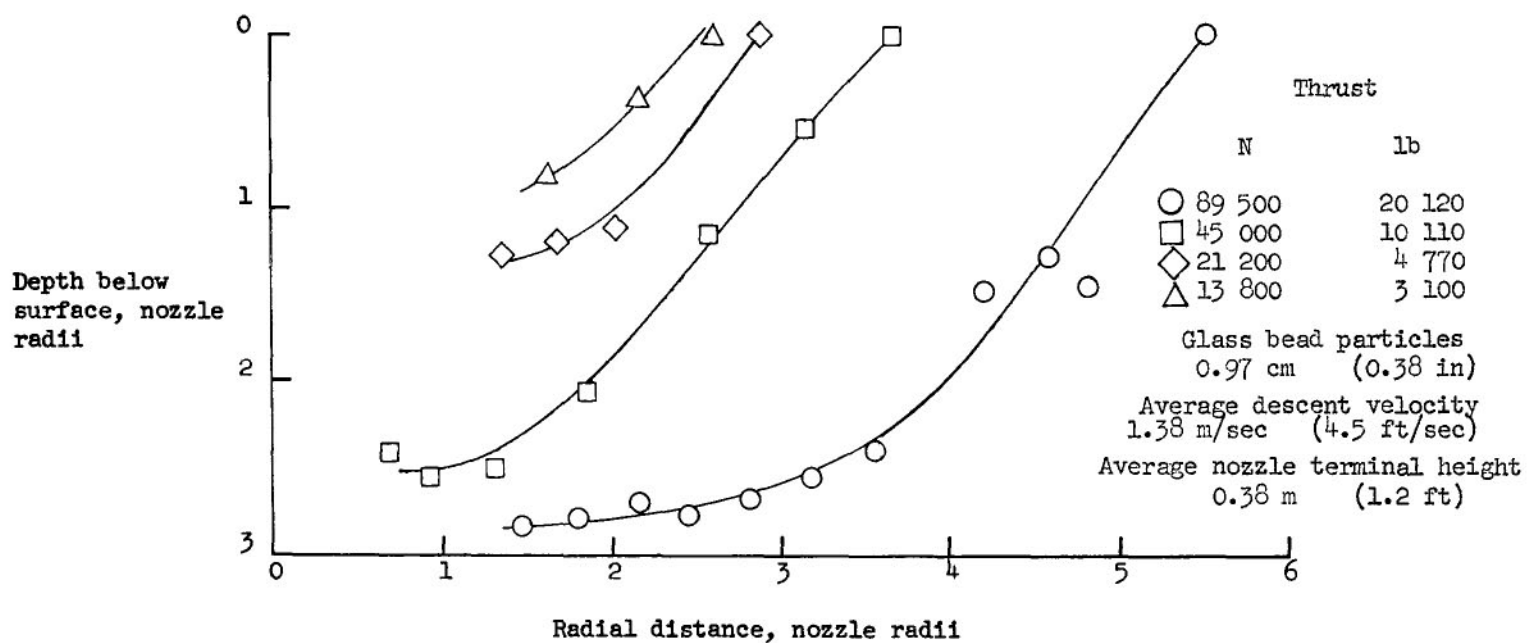Figure 17.- Effect of descent velocity on crater profile at end of descent.

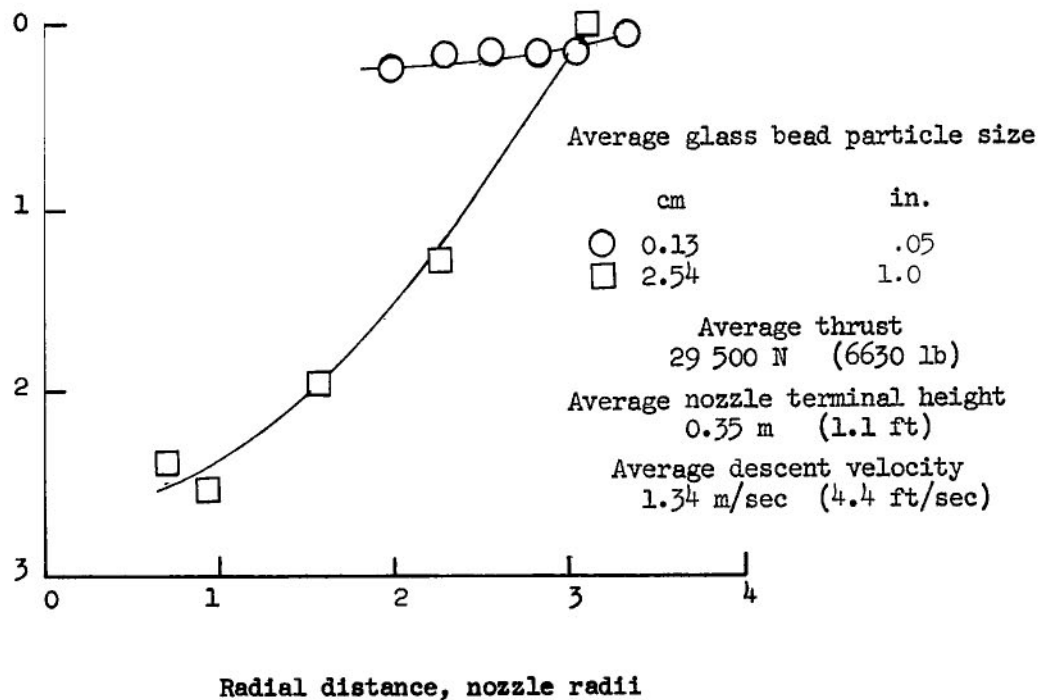Figure 18.- Effect of thrust on crater profile at end of descent.

Figure 19.- Effect of particle size on crater profile at end of descent.

Descent Conditions

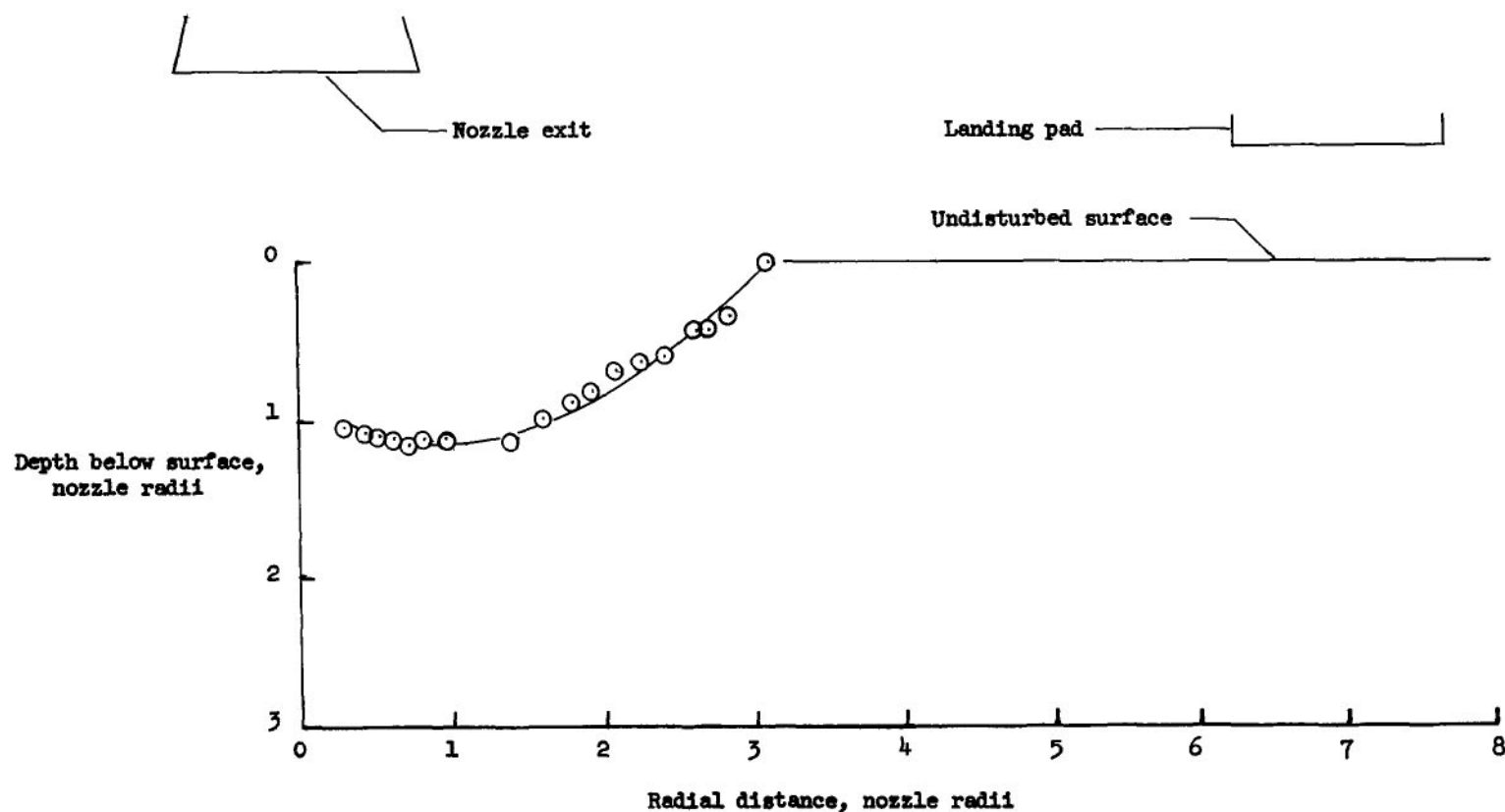|		
Thrust cut-off height	0.78 m	2.6 ft
Thrust	10 800 N	2420 lb
Descent velocity	0.61 m /sec	2.0 ft /sec
Particle size	2.54 cm	1.0 in.

Figure 20.- Crater profile for a typical LM descent. Crater contained 6.20 cubic meters (219 cubic feet) of material.

"The aeronautical and space activities of the United States shall be conducted so as to contribute . . . to the expansion of human knowledge of phenomena in the atmosphere and space. The Administration shall provide for the widest practicable and appropriate dissemination of information concerning its activities and the results thereof."

— NATIONAL AERONAUTICS AND SPACE ACT OF 1958

NASA SCIENTIFIC AND TECHNICAL PUBLICATIONS

TECHNICAL REPORTS: Scientific and technical information considered important, complete, and a lasting contribution to existing knowledge.

TECHNICAL NOTES: Information less broad in scope but nevertheless of importance as a contribution to existing knowledge.

TECHNICAL MEMORANDUMS: Information receiving limited distribution because of preliminary data, security classification, or other reasons.

CONTRACTOR REPORTS: Scientific and technical information generated under a NASA contract or grant and considered an important contribution to existing knowledge.

TECHNICAL TRANSLATIONS: Information published in a foreign language considered to merit NASA distribution in English.

SPECIAL PUBLICATIONS: Information derived from or of value to NASA activities. Publications include conference proceedings, monographs, data compilations, handbooks, sourcebooks, and special bibliographies.

TECHNOLOGY UTILIZATION PUBLICATIONS: Information on technology used by NASA that may be of particular interest in commercial and other non-aerospace applications. Publications include Tech Briefs, Technology Utilization Reports and Notes, and Technology Surveys.

Details on the availability of these publications may be obtained from:

SCIENTIFIC AND TECHNICAL INFORMATION DIVISION

NATIONAL AERONAUTICS AND SPACE ADMINISTRATION
Washington, D.C. 20546